NTNU
Norwegian University of
Science and Technology

Chaotic Vortex Dynamics in Bose-Einstein Condensates

Tiantian Zhang

Master of Science in Physics and Mathematics
Submission date: August 2017
Supervisor: Jon Andreas Støvneng, IFY
Co-supervisor: Thomas Busch, Okinawa Institute of Science and Technology Graduate University

Norwegian University of Science and Technology
Department of Physics

To all the good memories on this beautiful island

Abstract

Quantum vortices in superfluid Bose–Einstein condensates (BECs) are excellent candidates for studying hydrodynamic phenomena, such as turbulence and chaos, due to the quantization of vortex circulation and the absence of dissipation in BECs. Since the early 2000s, many experimental groups have successfully observed vortices in dilute atomic BECs.

This work mainly focuses on creating quantum chaos with a few vortices in a two-dimensional BEC of Rubidium-87. We use graphics processing unit (GPU) computing methods to simulate our BEC trapped inside a harmonic potential with tight trapping in one direction. The quantum vortices are created by rotating the condensate. After generating the ground state of the BEC with a small number of singly charged vortices with positive phase winding, we imprint a 4π phase winding on top of one vortex in the opposite orientation to that of the original vortex. This phase imprinting annihilates the preexisting vortex and creates a new singly-charged vortex with negative phase winding. Due to the high resolution of our system and an excellent vortex tracking algorithm, the location of phase imprinting can be delicately controlled.

Both the individual vortex dynamics and the dynamics of the entire system of vortices after flipping a vortex have shown strong signs of chaos. This chaotic nature is further confirmed both qualitatively and quantitatively by employing two chaos indicators on our numerical results. These chaos indicators are the Lyapunov exponent spectrum and the Smaller ALignment Index (SALI). The Lyapunov exponent remains positive and converges to a positive value during an experimentally realistic time period, which is the smoking gun for chaotic behaviour.

Sammendrag

Kvantevirvler i superflytende Bose–Einstein kondensater er utmerkede kandidater for forskning på hydrodynamiske fenomener, som for eksempel turbulens og kaos, siden de har kvantisering av virvling og fravær av viskositet. Siden tidlig på 2000-tallet har mange eksperimentelle grupper rapportert vellykkede observasjoner av virvler i fortynnede atomiske Bose–Einstein kondensater.

Dette studiet fokuserer hovedsakelig på å skape kaotisk oppfrsel ved hjelp av kvantevirvler i to-dimensjonale Bose–Einstein kondensater av Rubidium-87. Vi benytter grafikkprosessorprogrammering for å effektivisere datasimulering. Vi simulerer et roterende Bose–Einstein kondensat som befinner seg i et tre-dimensjonalt harmonisk potensiale hvor fangstfrekvensen i en retning er mye hyere enn i de to andre retningene. Etter at grunntilstanden av Bose–Einstein kondensater med få kvantevirvler er funnet ved hjelp av Fourier-splittingmetoden, avsettes en fase av 4π i motsatt retning av den originale virvelen, også kjent som virvelvending. Dette vil annihilere den originale virvelen og danne en ny kvantevirvel med motsatt sirkulasjon. På grunn av hy opplsning på systemet vårt og en utmerket algoritme for virvelsporing, kan posisjonen til faseavsettingen bli kontrollert med stor nyaktighet.

Vi studerer bevegelsen av virvlene i det samtroterende referansesystemet i noen tidsperioder etter at virvelvendingen har funnet sted. Både dynamikken av individuelle kvantevirvler og dynamikken til hele systemet av kvantevirvler har vist tegn til kaos. Denne kaotiske oppfrselen er bekreftet både kvalitativt og kvantitativt ved å benytte to kaosindikatorer på våre numeriske resultater. De benyttede kaosindikaterene er Lyapunov eksponent spektrum og den mindre justeringsindeksen. Lyapunov eksponent spektrum har vært det determinderende beviset for kaotisk oppfrsel av få kvantevirvler i Bose–Einstein kondensater fanget i et harmonisk potensiale.

Preface

Incredibly many thanks to my supervisor Professor Thomas Busch, for offering me the opportunity to conduct my Master project at Okinawa Institute of Science and Technology, Graduate University (OIST), along with many valuable help that you have provided. It is been an amazing experience. Lots of thanks to Angela White for close supervision and all the support, especially during the last stage of finishing this dissertation. I wouldn't have been able to complete this without your help. And thank you for all the delicious cakes that you have made. They made my experience here so much more fulfilling. Lots of thanks to James Schloss for all the time you have spent on helping me with GPU computing. A big thanks to Thomas Forgarty, Kien Pham, Rashi Sachdeva and Matthew Edmond for proofreading this dissertation.

Tiantian Zhang

Okinawa, 2017

Table of Contents

List of Tables

List of Figures

Abbreviations

Symbol	definition
BEC	Bose-Einstein Condensate
GPE	Gross-Pitaevskii Equation
GPU	Graphics Processing Unit

Nomenclatures

symbol	definition	value
a_s	s-wave scattering length	$4.76 \cdot 10^{-9}\mathrm{m}$
$\hbar$	the reduced Planck's constant	$1.0546 \cdot 10^{-34}\mathrm{m}^2 \cdot \mathrm{kg/s}$
m	atomic mass of ^{87}Rb	$1.443161 \cdot 10^{-25}\mathrm{kg}$

Chapter 1

Introduction

The motivation behind this work is to study the dynamics of few vortex systems in Bose–Einstein condensates and to identify whether the vortex dynamics induced by a perturbation to their initial position, is chaotic or not. Our analyses are based on the numerical solutions of the time dependent Gross-Pitaevskii equation, whose nonlinearity makes solving the equation analytically very challenging. This project is conducted as a part of the Master program in Applied Physics at the Norwegian University of Science and Technology (NTNU). The research for this dissertation has been carried out at the Okinawa Institute of Science and Technology Graduate University (OIST).

Classical chaos and turbulence are very common hydrodynamic phenomena, however they are hard to control or predict. How chaos behaves in quantum mechanics is a question that has been raised since the early 1900s. An extensive study of quantum chaos wasn't performed until the second half of the 1900s when ultracold systems were realised experimentally. Recently quantum chaos has been successfully observed with ultracold Erbium atoms (Frisch et al. (2014)). Contrary to classical hydrodynamics, there exist quantum fluids that are inviscid. This greatly simplifies the mechanics and may provide a shortcut to understand the nature of chaos and turbulence in the classical world.

Chapter 2 contains some theoretical background of the system that we have studied, namely dilute atomic Bose–Einstein condensates. We will cover the derivation of Bose–Einstein condensation, as well as how they were realised experimentally, the Gross-Pitaevskii equation that governs the time evolution of Bose–Einstein condensates and the formation of quantum vortices, which is the basis of this study on quantum dynamics in Bose-Einstein condensates.

In Chapter 3, the numerical methods that have been used to simulate our system are introduced. The Fourier split operator method is a numerical method for calculating the time evolution of the Gross-Pitaevskii equation. We have been running our simulations using Graphics prosessiing unit (GPU) computing techniques, which greatly speeds up the

running time and allows us to run multiple simulations simultaneously. We implement a very useful algorithm to track vortices. This allows us to keep track of the movement of each individual vortex from one time frame to the next, which is crucial for the study of vortex dynamics.

Chapter 4 covers the definition and general application of two chaos indicators, the Lyapunov exponent and the small alignment indicator. We apply these chaos indicators in order to qualitatively and quantitatively identify whether or not the vortex dynamics are chaotic, when subject to perturbations in their initial conditions.

In Chapter 5 and 6, our results and the corresponding analyses performed on the simulation data are presented. We divide our results into two main branches, ordered and chaotic dynamics. During the course of this project, we have studied few vortex systems with up to 6 vortices, while our main focus is on systems with 4 vortices.

During this work, the possibility of alternative representations of Bose–Einstein condensates, useful for interpreting the simulated data, have been investigated. In particular, we compute both the momentum distribution and the Wigner function, or quasi-probability distribution of the condensate. These representations are presented in Chapter 7. We have applied these representations to our numerical data, as well as an ansatz for the condensate wavefunction with a vortex.

The last chapter summarises this work, and also presents an outlook on the potential further development of this work in the future.

Chapter 2

Background

Quantum vortices in Bose–Einstein condensates (BECs) are stable due to a conserved topological phase. With their quantised circulation, quantum vortices make an excellent system for studying turbulence and chaos compared to classical systems, where continuity and dissipation complicate the dynamics significantly. The main goal of this work is to study the dynamics of quantum vortices in a rotating quasi-two-dimensional Bose–Einstein condensate of a dilute ^{87}Rb gas, confined within a three-dimensional harmonic trap where confinement in one direction is much tighter than in the other two. In this chapter, we will start with an introduction to Bose–Einstein condensation and the creation of quantum vortices. Later on in this chapter, we will also briefly cover superfluidity and its defining features.

2.1 Motivation

The development of ultracold atomic physics sprouted in the late 1990s thanks to the experimental realisation of ultracold atoms followed closely by the creation of Bose–Einstein condensates. In 1997 Steven Chu, Claude Cohen-Tannoudji and William D. Phillips received the Nobel Prize in physics for their work on the cooling and trapping of atoms with laser light (Nobelprize.org (1997)). In 2001 Eric Cornell, Wolfgang Ketterle and Carl Wieman were awarded the Nobel prize in physics for the experimental realisation of Bose–Einstein condensation in dilute gases of alkali atoms (Nobelprize.org (2001)). Shortly after in 2003, Alexei A. Abrikosov, Vitaly L. Ginzburg and Anthony J. Leggett were awarded the Nobel prize in physics for their contribution to the theory of superconductors and superfluids (Nobelprize.org (2003)). Ever since, research in ultracold atomic physics has been extensively explored across a range of wide applications, from quantum information technologies to the study of elementary physics laws.

2.1.1 Experimental background on ultracold atoms

Ultracold atoms are typically referred to as atoms at a temperature range around nano-Kelvin. At this temperature, the quantum mechanical properties of atoms are very pronounced, hence very crucial for their behaviour. Cooling atoms to nano-Kelvin temperatures requires advanced experimental techniques. We are going to introduce some basic experimental techniques that have been used to cool down atoms to almost absolute zero.

Laser cooling is the most commonly used technique for atomic cooling. This technique utilises the fact that atoms absorb photons which are on resonance with the energy difference between two energy states and re-emit a photon in a random direction afterwards.
In practice, one uses two counter-propagating laser beams to slow down atomic clouds

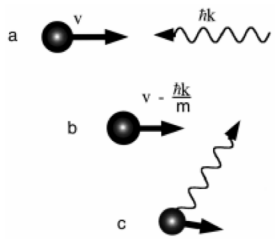

Figure 2.1: (a) An atom with velocity v encounters a photon with momentum $\hbar k = h/\lambda$; (b) After absorbing the photon, the atom is slowed by $\hbar k/m$; (a) After re-emitting a photon $\hbar k$ in a random direction, on average the atom is slowed down by $\hbar k/m$ relative to (a). Figure reprinted from Phillips (1998).

in one direction. For three dimensional (3D) cooling, three pairs of counter-propagating laser beams are needed. The laser beam is slightly red-detuned compared to the energy difference between the two hyperfine states of the atoms, so that atoms moving towards the laser source get slowed down. This type of laser cooling is also known as Doppler cooling. The lasers are on resonance with the atoms when the atoms are moving towards the laser source and hence slow down atoms in that direction, as depicted in figure 2.1.

Most of the time, cooling and trapping both need to be present for the realisation of ultracold atoms. There are multiple traps available today, such as Ioffe–Pritchard traps (Pritchard (1983)), optical dipole traps (Grimm et al. (2000)) and magneto-optical traps (Steane et al. (1992)). Furthermore, in order to reach Bose–Einstein condensation, evaporative cooling techniques have been put into use to depopulate the atoms in higher momentum states to further cool the atomic cloud. Many experiments have proven ultracold atoms to be useful for a range of applications, for instance Bloch et al. (2008), Fläschner et al. (2016) and Suchet et al. (2016).

2.2 Bose–Einstein condensation

The existence of Bose–Einstein condensates was first proposed in the 1907 by Einstein, following the work of Bose on the statistics of photons. Experiments with superfluid Helium (^{4}He) were considered as the first realisation of BEC. However the strong interatomic interactions among He atoms makes the occupancy number at zero-momentum level low, even at 0K. Searches for alternative candidates targeted alkali atoms, such as ^{1}H, ^{39}K and ^{85}Rb. In particular, H atoms were initially a popular candidate, due to their low mass and hence high condensation temperature. The first successful experiment realising BEC in a dilute gas was performed by Anderson et al. (1995).

2.2.1 Ideal Bose gas

Bosons, which refer to particles with integer spins, are not constrained by the Pauli exclusion principle. More than one boson can occupy the same quantum state. Their occupation number in different quantum states are governed by Bose statistics, with the mean occupation number of state ν expressed as

$$f^0(\epsilon_\nu) = \frac{1}{e^{(\epsilon_\nu - \mu)/k_B T} - 1}, \tag{2.1}$$

where ϵ_ν is the energy at state ν, k_B is the Boltzmann constant and μ is the chemical potential defined as $\mu = \frac{\partial E}{\partial N}$. Two other important quantities that can be derived from this are the mean energy

$$E = \sum_\nu \epsilon_\nu f^0(\epsilon_\nu), \tag{2.2}$$

and the mean particle number

$$N = \sum_\nu f^0(\epsilon_\nu). \tag{2.3}$$

In the case of an abundance of available quantum states, we can replace the finite sized summation over energy with an infinitesimal integration

$$N = \int_0^\infty d\epsilon f^0(\epsilon) g(\epsilon), \tag{2.4}$$

where $g(\epsilon)$ is the density of states at energy ϵ. Let us now look closely at the density of states of bosons in three-dimensional space. The total number of states available with energy less than $\epsilon = \frac{p^2}{2m}$ can be described as

$$G(\epsilon) = \frac{V}{(2\pi\hbar)^3} \frac{4}{3} \pi p^3, \tag{2.5}$$

where V is the volume of the system in real space confined in a three-dimensional box, and $(2\pi\hbar)^3$ is the unit volume per quantum state in 3D momentum space, derived from Heisenberg's uncertainty principle. Therefore the energy density of states is

$$g(\epsilon) = \frac{dG}{dE} = V \frac{2\pi(2m)^{3/2} V}{(2\pi\hbar)^3} \sqrt{\epsilon}. \tag{2.6}$$

2.2.2 Derivation of Bose–Einstein condensation

By integrating the Bose–Einstein distribution over energy,

$$N = \frac{2\pi(2m)^{3/2}V}{h^3}\int_0^\infty \frac{E^{1/2}}{e^{(E-\mu)/k_BT}-1}dE, \tag{2.7}$$

one obtains the occupation number

$$N = \frac{(2\pi mk_BT)^{3/2}V}{h^3}g_{3/2}(z), \tag{2.8}$$

where $z = e^{\mu/k_BT}$ and $g_\beta(z) = \sum_{p=1}^\infty z^p/p^\beta$, obtained from

$$\int_0^\infty \frac{x^\alpha}{e^x/z-1}dx = \Gamma(\alpha+1)g_{\alpha+1}(z). \tag{2.9}$$

The maximum value of $g_{3/2}(z)$ is reached when $z = 1$ (corresponding to $\mu = 0$, which is the maximum value of the chemical potential, which is always non-positive to avoid negative occupation numbers), giving $g_{\frac{3}{2}}(1) = \zeta(\frac{3}{2}) \simeq 2.612$. Plugging this into equation (2.8), we have

$$N_c = \frac{(2\pi mk_BT)^{3/2}V}{h^2}\zeta(\frac{3}{2}), \tag{2.10}$$

which is the critical occupation number of the ground state. The corresponding critical temperature is

$$T_c = \frac{h^2}{2\pi mk_B}\Big(\frac{N}{\zeta(3/2)}V\Big)^{3/2}. \tag{2.11}$$

When $T < T_c$ (and $N > N_c$), the excited states are largely suppressed. This implies that the fluid will undergo a phase transition and occupy the ground state, creating a Bose–Einstein condensate. In order to identify the fraction of condensed atoms, we use the expression

$$\frac{N_0}{N} = 1 - \frac{N_{\text{ex}}}{N}, \tag{2.12}$$

where $N = N_0 + N_{\text{ex}}$, N_0 is the number of particles in the ground state and N_{ex} is the number of particles occupying excited states. The condensate fraction can also be expressed in terms of temperatures as

$$\frac{N_0}{N} = 1 - \frac{T}{T_c}^{3/2}. \tag{2.13}$$

Particle wave nature

Using the definition of particle density, $n = N/V$, the criterion for BEC according to equation (2.8) becomes

$$n > \zeta\Big(\frac{3}{2}\Big)\Big(\frac{2\pi mk_BT}{h^3}\Big)^{\frac{3}{2}}. \tag{2.14}$$

The de Broglie wave length of a particle with mass m is defined as $\lambda_{\text{dB}} = h/p$, and for a thermal particle

$$p = \sqrt{2\pi m k_B T} \Rightarrow \lambda_{\text{dB}} = \sqrt{\frac{h^2}{2\pi m k_B T}}. \tag{2.15}$$

Hence equation (2.14) can be written as

$$n\lambda_{\text{dB}} > \zeta(\frac{3}{2}) \simeq 2.618. \tag{2.16}$$

This implies that the interparticle spacing ($d = n^{-1/3}$) must be smaller than the spatial spread of the particles wavefuncion. This overlap of wave packets is crucial for the formation of a BEC, where a macrostate wavefuntion which describes all particles in a BEC collectively exists.

2.2.3 Gross-Pitaevskii equation

Since solving the full many body dynamics of system of many quantum particles is an intractable problem, it is necessary to identify appropriate schemes to gain useful insight into these systems. In the low temperature regime, the typical particle densities of atomic condensate lie in the range of $10^{12} - 10^{15}\text{cm}^{-3}$, giving a mean spacing of $\sim 0.1 - 1\mu\text{m}$. The van der Waals interaction on the other hand has a range of the order of $n\text{m}$, rendering the effect very small. This allows us to model atomic condensate using mean field theory.

In a real dilute many particle system, the interparticle interactions (even though weak) should be included, which makes the Schrödinger equation a nonlinear equation.
N interacting atoms inside an external potential, V_{ext}, can be described by a many-body Hamiltonian given in second quantisation (occupation number representation) as

$$\hat{H} = \int d\boldsymbol{r}\hat{\Psi}^\dagger(\boldsymbol{r})\Big\{-\frac{\hbar^2}{2m}\nabla^2 + V_{\text{ext}}(\boldsymbol{r}) + \frac{1}{2}\int d\boldsymbol{r'}\hat{\Psi}^\dagger(\boldsymbol{r'})V(\boldsymbol{r}-\boldsymbol{r'})\hat{\Psi}(\boldsymbol{r'})\Big\}\hat{\Psi}(\boldsymbol{r}), \tag{2.17}$$

where $V(\boldsymbol{r}-\boldsymbol{r'})$ is the inter-particle interaction and $\hat{\Psi}^\dagger(\boldsymbol{r})$ and $\hat{\Psi}(\boldsymbol{r})$ are the creation and annihilation operators, respectively, of the Bose field. These field operators create (annihilate) a particle at a particular position in space. They are obtained by performing a basis transformation of creation and annihilation operators ($\hat{a}^\dagger, \hat{a}$) on the occupation number of a certain state,

$$\hat{a}_\nu|n_1, n_2, \cdots, n_\nu, \cdots\rangle = \sqrt{n_\nu}|n_1, n_2, \cdots, n_\nu - 1, \cdots\rangle, \tag{2.18}$$

$$\hat{a}_\nu^\dagger|n_1, n_2, \cdots, n_\nu, \cdots\rangle = \sqrt{n_\nu + 1}|n_1, n_2, \cdots, n_\nu + 1, \cdots\rangle, \tag{2.19}$$

where $n_\nu \in [0, \infty)$ for bosons. They satisfy the following lower boundary condition

$$\hat{a}^\dagger|0\rangle = |1\rangle, \hat{a}|0\rangle = 0, \tag{2.20}$$

where $|0\rangle$ denotes the state of the vacuum (occupation number).
First we recall a single particle with state $|\nu\rangle$

$$\phi_\nu(\boldsymbol{r}) = \langle\boldsymbol{r}|\nu\rangle, \tag{2.21}$$

then we project this onto the spatial coordinate basis

$$\phi(\boldsymbol{r}) = \sum_{\nu} \hat{a}_{\nu}\langle \boldsymbol{r}|\nu\rangle = \sum_{\nu} \hat{a}_{\nu}\phi_{\nu}(\boldsymbol{r}) \tag{2.22}$$

$$\phi^{\dagger}(\boldsymbol{r}) = \sum_{\nu} \langle \nu|\boldsymbol{r}\rangle \hat{a}^{\dagger}_{\nu} = \sum_{\nu} \phi^{*}_{\nu}(\boldsymbol{r})\hat{a}^{\dagger}_{\nu}. \tag{2.23}$$

$$\tag{2.24}$$

Recalling equation (2.36), the number density operator of a many-body system is represented as

$$\hat{n}(\boldsymbol{r}) = \hat{\Psi}^{\dagger}(\boldsymbol{r})\hat{\Psi}(\boldsymbol{r}), \tag{2.25}$$

and the total number of the system is

$$\hat{N} = \int d\boldsymbol{r}\hat{\Psi}^{\dagger}(\boldsymbol{r})\hat{\Psi}(\boldsymbol{r}). \tag{2.26}$$

The creation and annihilation field operators satisfy the commutation relations

$$[\hat{\Psi}(\boldsymbol{r}), \hat{\Psi}^{\dagger}(\boldsymbol{r'})] = \delta(\boldsymbol{r} - \boldsymbol{r'}), \quad [\hat{\Psi}^{\dagger}(\boldsymbol{r}), \hat{\Psi}^{\dagger}(\boldsymbol{r'})] = 0 \quad \text{and} \quad [\hat{\Psi}(\boldsymbol{r}), \hat{\Psi}(\boldsymbol{r'})] = 0. \tag{2.27}$$

Interatomic interactions typically depend strongly on interatomic distances. For dilute gases, this interaction can be described as an effective interaction in the form of a contact potential

$$V(\boldsymbol{r} - \boldsymbol{r'}) = g\boldsymbol{\delta}(\boldsymbol{r} - \boldsymbol{r'}), \tag{2.28}$$

where g is the interaction strength. In the low-momentum frame, the s-wave scattering dominates the scattering kinetics described by a single parameter, namely the scattering length

$$a_s = \frac{m_r}{2\pi\hbar^2}\int d\boldsymbol{r}V(\boldsymbol{r}), \tag{2.29}$$

where m_r is the reduced mass. If the two colliding atoms are of the same species, $m_r = m/2$. This expression is the Born approximation for the scattering length. Hence the interaction strength can be expressed as

$$g = \frac{4\pi\hbar^2 a_s}{m}. \tag{2.30}$$

Plugging this into equation (2.17), one gets

$$\hat{H} = \int d\boldsymbol{r}\hat{\Psi}^{\dagger}(\boldsymbol{r})[-\frac{\hbar^2}{2m}\nabla^2 + V_{\text{ext}}(\boldsymbol{r})]\hat{\Psi}(\boldsymbol{r}) + \frac{1}{2}g\int d\boldsymbol{r}\hat{\Psi}(\boldsymbol{r})\hat{n}(\boldsymbol{r})\Psi(\boldsymbol{r}). \tag{2.31}$$

The Heisenberg equation, which is an alternative description in quantum mechanics, states

$$i\hbar\frac{\partial}{\partial t}\hat{\Psi}(\boldsymbol{r}, t) = [\hat{\Psi}, \hat{H}], \tag{2.32}$$

which gives the time evolution of $\hat{\Psi}(\boldsymbol{r}, t) = e^{i\hat{H}t/\hbar}\hat{\Psi}(\boldsymbol{r})e^{-i\hat{H}t/\hbar}$. By plugging equation (2.17) into equation (2.32) and exploiting the commutation relation, one gets

$$i\hbar\frac{\partial}{\partial t}\hat{\Psi}(\boldsymbol{r}, t) = \Big[-\frac{\hbar^2}{2m}\nabla^2 + V_{\text{ext}}(\boldsymbol{r}) + \int d\boldsymbol{r'}\hat{\Psi}^{\dagger}(\boldsymbol{r'}, t)\hat{n}(\boldsymbol{r'})\Psi(\boldsymbol{r'}, t)\Big]\hat{\Psi}(\boldsymbol{r}, t). \tag{2.33}$$

Due to the macroscopic occupation of atoms in the ground state, the quantum field operator, $\hat{\Psi}$ can be expressed as

$$\hat{\Psi} = \Psi + \delta\hat{\Psi}, \tag{2.34}$$

where $\Psi = \langle\hat{\Psi}\rangle$ is the classical field order parameter (condensate) and $\delta\hat{\Psi}$ is the quantum fluctuation operator (non-condensate) and is negligible in the description of BECs. Thus replacing the quantum field operator, $\hat{\Psi}$, with the classical field order parameter, Ψ, one gets the time-dependent Gross-Pitavskii equation (GPE),

$$i\hbar\frac{\partial}{\partial t}\Psi(\boldsymbol{r},\boldsymbol{t}) = -\frac{\hbar^2}{2m}\nabla^2\Psi(\boldsymbol{r},t) + V_{\text{ext}}(\boldsymbol{r})\Psi(\boldsymbol{r},t) + g|\Psi(\boldsymbol{r},t)|^2\Psi(\boldsymbol{r},t). \tag{2.35}$$

The Hartree–Fock method (Slater (1951)) has been shown to be a good approximation for the wave function as a solution of the many-body Schrödinger equation, where low density and weak interparticle interactions apply. For these conditions, the correlations between particles are weak and hence a mean-field theory is justified. The Hartree–Fock (HF) approximation is formulated as

$$\Psi(\boldsymbol{r_1},\boldsymbol{r_2},\cdots,\boldsymbol{r_N}) = \prod_{i=1}^{N}\phi(\boldsymbol{r_i}), \tag{2.36}$$

where ϕ is the wave function of a single particle and Ψ is the total wave function of N particles. The HF approximation assumes that the wave function of each individual particle is independent of the location of the other particles. The standard normalisation condition for a single-particle wave function is

$$\int d\boldsymbol{r}|\phi(\boldsymbol{r})|^2 = 1. \tag{2.37}$$

The following normalisation condition is then satisfied;

$$\int d\boldsymbol{r}|\Psi(\boldsymbol{r})|^2 = N, \text{ where} \qquad \Psi(\boldsymbol{r}) = \sqrt{N}\phi(\boldsymbol{r}). \tag{2.38}$$

The expectation value of the Hamiltonian in equation (2.35) is

$$E = \int d\boldsymbol{r}\Big[\frac{\hbar^2}{2m}|\nabla\Psi(\boldsymbol{r})|^2 + V_{\text{ext}}(\boldsymbol{r})|\Psi(\boldsymbol{r})|^2 + \frac{N-1}{2N}g|\Psi(\boldsymbol{r})|^4\Big]. \tag{2.39}$$

The time-evolution of the Hamiltonian operator in the Heisenberg representation brings the system from the state $|N\rangle$ to $|N-1\rangle$,

$$\psi(\boldsymbol{r},t) = \langle N-1|\hat{\psi}(\boldsymbol{r})|N\rangle \propto e^{-i(E_N - E_{N-1})t/\hbar}. \tag{2.40}$$

When $N \gg 1$,

$$E_N - E_{N-1} \approx \mu \equiv \frac{\partial E}{\partial N}, \tag{2.41}$$

hence the time-dependent wave function can be expressed in the following way

$$\Psi(\boldsymbol{r},t) = \psi(\boldsymbol{r})e^{-i\mu t/\hbar}. \tag{2.42}$$

Plugging the equation above into the time-dependent GPE in equation (2.35), gives us the time-independent GPE

$$\Big\{ -\frac{\hbar^2}{2m}\nabla^2 + V_{\text{ext}}(\boldsymbol{r}) + g|\psi(\boldsymbol{r})|^2 \Big\}\psi(\boldsymbol{r}) = \mu\psi(\boldsymbol{r}). \tag{2.43}$$

In cases where the interparticle interactions are absent, $\mu = E$.

The ground state for trapped bosons

Assuming a three dimensional isotropic harmonic trap with $V = m\omega_0^2 r^2/2$ and the kinetic energy term, $K = \hbar^2/2mr^2$, the total energy of a particle is at its minimum when $V = K$. This leads to an expression for the characteristic quantum mechanical length for the harmonic oscillator,

$$a_{\text{osc}} = \Big(\frac{\hbar}{m\omega_0}\Big)^{1/2}. \tag{2.44}$$

2.2.4 The Thomas-Fermi approximation

The Thomas–Fermi approximation neglects the kinetic term in the GPE in equation (2.43), which is a reasonable assumption for repulsive interatomic interactions in the ultracold atom regime (~ 0K) when the interaction energy is much larger than the kinetic energy. Making the Thomas–Fermi approximation, equation (2.43) then becomes

$$[V(\boldsymbol{r}) + g|\psi(\boldsymbol{r})|^2]\psi(\boldsymbol{r}) = \mu\psi(\boldsymbol{r}). \tag{2.45}$$

Inside the atomic cloud radius (non-zero atomic density $\Psi(\boldsymbol{r}) > 0$), this gives us

$$n(\boldsymbol{r}) = |\psi(\boldsymbol{r})|^2 = \frac{\mu - V(\boldsymbol{r})}{g}. \tag{2.46}$$

We defined $n(\boldsymbol{r}) = 0$ ($\Psi(\boldsymbol{r}) = 0$) for $V(\boldsymbol{r}) \geqslant \mu$. The potential of a harmonic trap is,

$$V(\boldsymbol{r}) = \sum_{i=x,y,z} \frac{1}{2} m\omega_i^2 r_i^2. \tag{2.47}$$

By plugging the equation above into the boundary condition, the extension of the cloud, or condensate radius, can be obtained to be

$$R_i = \sqrt{\frac{2\mu}{m\omega_i^2}}, \qquad i = x, y, z, \tag{2.48}$$

and the geometric mean of the cloud extension is

$$\bar{R} = \sqrt{\frac{2\mu}{m\bar{\omega}^2}}, \tag{2.49}$$

where $\bar{\omega} = \prod_{i=x,y,z} \omega_i^{\frac{1}{3}}$ is the geometric mean of the trap frequencies. When $\omega_z \gg \omega_\perp$, the condensate is much more tightly confined in the $z-$direction and has a pancake shape. One can rewrite the 3D complex order parameter $\Psi(\boldsymbol{r}) = \Psi(x, y, z)$ as $\Psi(\boldsymbol{r}) = \Psi(x, y)$ describing two-dimensional (2D) BECs by integrating over the z-direction,

$$\Psi(\boldsymbol{r}) = \psi(x, y)\Phi(z). \tag{2.50}$$

Correspondingly, the strength of mean field potential due to interatomic interactions, $g_{2\text{D}}$, can be obtained by integrating g in the $z-$direction and taking the ground state wave function $\phi(z)$ to be in the form of a Gaussian distribution,

$$\Phi(z) = \Big(\frac{1}{\pi a_z^2}\Big)^{\frac{1}{4}} \exp(-\frac{z^2}{2a_z^2}), \tag{2.51}$$

where $a_z = \sqrt{\frac{\hbar}{m\omega_z}}$, is the characteristic harmonic oscillator length in the z-direction. The resulting interaction strength $g_{2\text{D}}$, is then

$$g_{2\text{D}} \equiv g \int_{-\infty}^{\infty} dz |\Phi(z)|^4 = \frac{g}{\sqrt{2\pi} a_z} = \frac{\sqrt{8\pi}\hbar^2 a_s}{m a_z}, \tag{2.52}$$

and we have used that

$$\int_{-\infty}^{\infty} dz \Big(\frac{1}{\pi a_z^2}\Big) e^{-2z^2/a_z^2} = \frac{1}{\sqrt{2\pi} a_z}. \tag{2.53}$$

The corresponding Hamiltonian of a 2D BEC can then be expressed as

$$i\hbar \frac{\partial}{\partial t}\psi(x, y) = \big[-\frac{\hbar^2}{2m}\nabla_\perp^2 + V(x, y) + \frac{g}{\sqrt{2\pi} a_z}\big]\psi(x, y), \tag{2.54}$$

where $\nabla_\perp^2 = \partial_x^2 + \partial_y^2$. In the Thomas–Fermi-approximation regime, the atomic density of the quasi-2D trapped BEC inside a quadratic trap has a very simple solution

$$n(\boldsymbol{r}) = n(0)\Big(1 - \sum_i \frac{r_i^2}{R_i^2}\Big), \qquad i = x, y, \tag{2.55}$$

where $n(0) = \frac{\mu}{g_{2\text{D}}}$. By applying $\int d_0^{R_x,R_y} \boldsymbol{r} n(\boldsymbol{r}) = N$, we can obtain the following expression for the chemical potential

$$\mu = \frac{3N g_{2\text{D}}}{R_x R_y}. \tag{2.56}$$

2.3 Rotating condensate

For a rotating BEC confined inside a harmonic trap, instead of working in the laboratory frame, we change our reference system to co-rotate with the external trapping potential. The GPE then has the following form

$$i\hbar \frac{\partial}{\partial t}\Psi(\boldsymbol{r}, t) = \Big(-\frac{\hbar^2}{2m}\nabla^2 + V(\boldsymbol{r}) - \boldsymbol{\Omega} \cdot \hat{\boldsymbol{L}} + g|\Psi(\boldsymbol{r}, t)|^2\Big)\Psi(\boldsymbol{r}, t), \tag{2.57}$$

where $\boldsymbol{\Omega}$ is the angular velocity of the external trap relative to the lab frame and $\hat{\boldsymbol{L}}$ is the angular momentum operator. The corresponding energy of the GPE in the rotating frame (where the rotating axis is along the z-direction, $\Omega_x = \Omega_y = 0$) is

$$E = \int d\boldsymbol{r}\Big[\frac{\hbar^2}{2m}|\nabla\Psi(\boldsymbol{r})|^2 + V(\boldsymbol{r})|\Psi(\boldsymbol{r})|^2 + \frac{1}{2}g|\Psi(\boldsymbol{r})|^4 - \Omega_z\Psi^*(\boldsymbol{r})\hat{L}_z\Psi(\boldsymbol{r})\Big]. \quad (2.58)$$

According to this equation, for nonzero Ω_z, the system favours nonzero angular momentum in the z-direction. That is, the nucleation of quantum vortices is preferable in rotating BECs. The angular momentum of the quasi-2D rotating atomic cloud is denoted as

$$\langle\hat{L}_z\rangle = i\hbar\int d\boldsymbol{r}\Psi^*\left(y\frac{\partial}{\partial x} - x\frac{\partial}{\partial y}\right)\Psi, \quad (2.59)$$

where $\hat{L}_z = y\hat{p}_x - x\hat{p}_y$.

2.3.1 Quantum vortices

Quantum vortices are a type of elementary excitation in a superfluid, as well as a characteristic signature of superfluidity. In 2000, quantum vortices were observed experimentally in a stirred atomic ^{87}Rb BEC (Madison et al. (2000)). Analytically, their existence can be understood from the time-dependent GPE. In order to understand better the rule the complex wave function, Ψ, plays for quantum vortices and to connect the condensate to the physics of fluids, it is instructive to use the Madelung transformation, $\Psi = \sqrt{n}e^{i\theta}$, to recast equation 2.35 in terms of the atomic density distribution $n(\boldsymbol{r},t) = |\psi(\boldsymbol{r},t)|^2$, and the phase of the wavefunction, $\theta(\boldsymbol{r},t) = \Im(\Psi(\boldsymbol{r},t))/\Re(\Psi(\boldsymbol{r},t))$.
The continuity equation can be derived from the time-dependent GPE by multiplying it by ψ^* and then subtracting the complex conjugate of the resulting equation. We then get the Euler equation,

$$\frac{\partial}{\partial t}|\Psi|^2 + \frac{\hbar}{2mi}\nabla(\Psi^*\nabla\Psi - \Psi\nabla\Psi^*) = 0. \quad (2.60)$$

The continuity equation typically takes the following form, which is also known as the mass conservation law,

$$\frac{\partial}{\partial t}n + \nabla(n\boldsymbol{v}) = 0, \quad (2.61)$$

where $\boldsymbol{v}$ is the flow velocity in the fluid. By comparing this to equation (2.60), we see that the velocity field of the condensate can be expressed as

$$\boldsymbol{v} = \frac{\hbar}{2mi}\frac{\Psi^*\nabla\Psi - \Psi\nabla\Psi^*}{|\Psi|^2}. \quad (2.62)$$

The velocity field in equation (2.62) is then

$$\boldsymbol{v} = \frac{\hbar}{m}\nabla\theta. \quad (2.63)$$

Note that $\nabla\times\boldsymbol{v} = 0$, meaning that the flow is irrotational.

The circulation along a closed curve C is defined as

$$\Gamma = \oint_C \boldsymbol{v} \cdot d\boldsymbol{l}. \tag{2.64}$$

If $\boldsymbol{v}$ is a continuously differentiable vector field, then the following applies;

$$\Gamma = \oint_A \nabla \times \boldsymbol{v} d\boldsymbol{A} = \frac{\hbar}{m} \oint_A \nabla \times \nabla\theta d\boldsymbol{A} = 0. \tag{2.65}$$

This means that the BEC can not contain rotational flow, unless there's a singularity in the vector field. The circulation around a singularity is

$$\Gamma = \frac{\hbar}{m} \oint_C \nabla\theta d\boldsymbol{l} = \frac{\hbar}{m}(\theta_2 - \theta_1) = \frac{\hbar}{m}\Delta\theta, \tag{2.66}$$

where $\Delta\theta$ is the change of the phase of the wave function after circulating around a singularity in a closed curve. Due to the single valuedness of the condensate wave function ,

$$\Delta\theta = 2\pi l, \quad l \in \mathbb{Z}. \tag{2.67}$$

In the case of an homogeneous rotation along the $z-$direction, the azimuthal velocity is of the most interest, as

$$v_\vartheta = \frac{\hbar}{m}\nabla\theta = \frac{\hbar}{m}\frac{1}{r}\frac{\partial}{\partial\vartheta}\theta = \frac{\hbar}{m}\frac{l}{r} \qquad \propto \frac{1}{r}, \tag{2.68}$$

where r is the scalar radius from the vortex core. The kinetic term of a vortex is then $\propto \frac{n}{r^2}$ and this means that in order to prevent divergence of the kinetic energy to infinity when we approach the vortex core ($r = 0$), the atomic density has to be zero there.

2.3.2 Creating quantum vortices experimentally

In a superfluid BEC, a vortex can nucleate as a form of excitations when the condensate's angular velocity exceeds the Landau critical velocity, although in practice, this value will deviate somewhat from the analytically predicted one. It's been shown in Madison et al. (2000) that this is indeed realised for Rb BEC. Many other experimental groups have also successfully demonstrated this ever since.

The healing length

Just as how the balance between the kinetic term and the external trapping potential defines the spatial spread of the atomic density inside the cloud, the balance between the kinetic term and the interatomic interaction term defines the depletion length over which the density goes from zero at the vortex core to the bulk condensate density (far away from the core). This distance is often referred to as the healing length, which is also in practice the size of a vortex. The healing length at the centre of the condensate is

$$\xi = \sqrt{\frac{\hbar^2}{2mn_0 g}}, \tag{2.69}$$

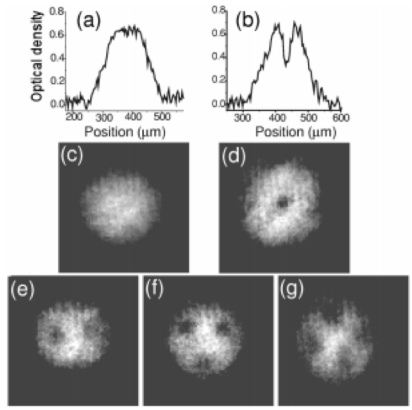

Figure 2.2: Transverse absorption images of a Bose–Einstein condensate stirred with a laser beam. The rotation frequency $\Omega/2\pi$ is, respectively (c) 145 Hz (0 vortex), (d) 152 Hz (1 vortex), (e) 169 Hz (2 vortices), (f) 163 Hz (3 vortices) and (g) 168 Hz (4 vortices). In (a) and (b) the variation of the optical thickness of the cloud along the horizontal transverse axis is shown for images (c) and (b). This figure is reprinted from Madison et al. (2000).

where $n_0 = |\Psi(\boldsymbol{r} = 0)|^2$ is the atomic density at the centre of the trapped atomic cloud and g is to be replaced by $g_{2\mathrm{D}}$ for a 2D BEC.

Properties of a single vortex

Consider a single vortex on the symmetry-axis with charge l. The wave function around the vortex core can be expressed as

$$\psi(\boldsymbol{r}) = f(\rho, z)e^{il\theta}, \tag{2.70}$$

and accordingly the corresponding energy is

$$E = \int d\boldsymbol{r}\Big\{\frac{\hbar^2}{2m}\Big[\Big(\frac{\partial f}{\partial \rho}\Big)^2 + \Big(\frac{\partial f}{\partial z}\Big)^2\Big] + \frac{\hbar^2}{2m}l^2\frac{f^2}{\rho^2} + V(\rho, z)f^2 + \frac{g^2}{2}f^4\Big\}, \tag{2.71}$$

where the second term is the kinetic energy term due to the azimuthal motion around the axis and $\hbar^2 l^2 f^2/2m\rho^2 = mf^2 v_\vartheta^2/2$. In addition we can plug equation (2.70) into the time-independent GPE to get an expression for f,

$$-\frac{\hbar^2}{2m}\Big[\frac{1}{\rho}\frac{\partial}{\partial \rho}\Big(\rho\frac{\partial f}{\partial \rho}\Big) + \frac{\partial^2 f}{\partial z^2}\Big] + \frac{\hbar^2}{2m\rho^2}l^2 f + V(\rho, z)f + gf^3 = \mu f. \tag{2.72}$$

For an on-axis vortex in a harmonically trapped atomic cloud where the Thomas–Fermi approximation is valid,

$$\frac{\xi_0}{R} = \frac{\hbar\omega_\perp}{2\mu}, \tag{2.73}$$

which means that the size of the vortex is much smaller than the extension of the atomic cloud, or in other words, the energy contribution of the excitation due to the density variation around the vortex core and the interatomic interations are negligible compared to the chemical potential. We only need to consider the azimuthal kinetic energy as the vortex energy, which can be expressed as

$$\epsilon_v \simeq \int_0^R 2\pi\rho d\rho \frac{l^2\hbar^2 n}{2m\rho^2} \simeq n(0)\frac{\pi l^2\hbar^2}{m}\ln\frac{R}{|l|\xi_0} \tag{2.74}$$

per unit length. This implies that l number of singly charged vortices are energetically favourable over a single vortex with charge l. The total angular momentum of a singly charged vortex within a 3D anisotropic harmonic potential (tight confinement in $z-$direction) is expressed as

$$\begin{aligned} L = N\hbar &= \hbar\int dn(\boldsymbol{r}) = n(0,0)\hbar\int_{-Z}^{Z} dz\int_0^R 2\pi\rho\Big(1-\frac{\rho^2}{R^2}-\frac{z^2}{Z^2}\Big) \\ &= \frac{8\pi}{15}n(0,0)R^2Z\hbar, \end{aligned} \tag{2.75}$$

where Z is the extension of the atomic cloud in the z-direction. As we will discuss later, one way of creating vortices experimentally is with a rotating trap. In this case, instead of working in the laboratory frame, it's more convenient to work in the frame co-rotating with the trap potential. The energy in this rotating reference frame is then

$$E' = E - \boldsymbol{\Omega}\cdot\boldsymbol{L}, \tag{2.76}$$

were $\boldsymbol{L}$ is the angular momentum of the system and $\boldsymbol{\Omega}$ is the rotation frequency of the trap relative to the lab frame. Due to the quantisation of energy for an excited state, only when a certain critical angular velocity, Ω_c, is exceeded will the excited state be energetically favourable. This critial angular velocity is given by

$$\Omega_c = \frac{E_L - E_0}{L}, \tag{2.77}$$

where E_L is the energy of the condensate with angular momentum L, and E_0 is the ground state energy of the condensate ($L = 0$). For the specific case where the excitation is a vortex along the rotation axis, the critical angular velocity of a particle at the edge of the cloud with angular momentum $\hbar$ is (Fetter (2009))

$$\Omega_c = \frac{5}{2}\frac{\hbar}{mR^2}\ln\Big(\frac{0.671R}{\xi_0}\Big), \tag{2.78}$$

or more qualitatively,

$$\Omega_c \sim \omega_0\Big(\frac{a_{\text{osc}}}{R}\Big)^{2/3}. \tag{2.79}$$

For a singly charged off-axis vortex in a 3D trapping potential at a distance b from the rotation axis ($z-$axis), the corresponding energy is

$$E = \frac{4\pi\hbar^2 n(0,0)Z}{3m}\ln\Big(\frac{R}{\xi_0}\Big)\Big(1-\frac{b^2}{R^2}\Big)^{3/2}, \tag{2.80}$$

and the corresponding angular momentum is

$$L = N\hbar\Big(1 - \frac{b^2}{R^2}\Big)^{5/2}, \tag{2.81}$$

which decreases with distance from the rotation axis. More details on the derivation of the above expressions can be found in Section 9.3.2 of Pethick and Smith (2008).

Vortex arrays

After the angular velocity of the rotating condensate exceeds the critical angular velocity, exictations in the form of vortices start to nucleate. Increasing the angular velocity further, more than one vortex will start to nucleate. The location of vortices formed has been calculated in Butts and Rokhsar (1999). The Hamiltonian of the system in the rotating frame is given by

$$\begin{aligned} H' &= H - \boldsymbol{\Omega}\cdot\boldsymbol{L} \\ &= \sum_{i=1}^{N}\Big(\frac{\boldsymbol{p_i}^2}{2m} + V(r_i) - \boldsymbol{\Omega}\cdot(\boldsymbol{r_i}\times\boldsymbol{p_i})\Big) + g\sum_{i<j}\delta(\boldsymbol{r_i}-\boldsymbol{r_j}) \\ &= \sum_{i=1}^{N}\Big(\frac{(\boldsymbol{p_i} - m\boldsymbol{\Omega}\times\boldsymbol{r_i})^2}{2m} + V(r_i) - \frac{m}{2}(\boldsymbol{\Omega}\times\boldsymbol{r_i})^2\Big) \\ &+ g\sum_{i<j}\delta(\boldsymbol{r_i}-\boldsymbol{r_j}). \end{aligned} \tag{2.82}$$

It's straight forward to see that the minimum value of the first term is reached when $\boldsymbol{p_i} = \boldsymbol{\Omega}\times\boldsymbol{r_i}$, which is rigid body rotation. The corresponding velocity field is $\boldsymbol{v_i} = \frac{\boldsymbol{\Omega}\times\boldsymbol{r_i}}{2m}$ and $\boldsymbol{\nabla}\times\boldsymbol{v_i} = 2\boldsymbol{\Omega}$. However, in a superfluid, this is only physically possible in the presence of singularities, i.e. vortices. A uniform array of vortices in the condensate residing in the plane perpendicular to the rotation axis (e.g. in the z-direction) approximates the velocity field of rigid body rotation. The number density of vortices in the condensate is

$$n_V = \frac{2m\Omega_z}{h} = \frac{1}{\pi a_{\Omega_z}{}^2}, \tag{2.83}$$

where a_Ω is the intervortex spacing, given by

$$a_\Omega = \sqrt{\frac{\hbar}{m\Omega_z}}. \tag{2.84}$$

2.4 Superfluidity

In contrast to the definition of BEC, superfluidity is a rather conventional concept that's been used to describe fluids that present certain features. The most common known property of superfluids is the frictionless flow and secondly it's unresponsiveness to low angular velocities. Even though the connection between BEC and superfluidity has been

made since back in 1938 by London based on Allen (1938) and Kapitza (1938), the correspondence between them is not yet complete. In Leggett (1999), a more clear distinction between these two phenomena has been given.

A commonly used picture for describing a superfluid is a two-fluid model where one of them is the normal fluid and the other is the ideal fluid. In particular the two-fluid model was initially developed in association with the superfluid Helium-4. The normal fluid is usually referred to as excitations induced either kinetically or thermally. For an excitation to be created kinetically, a critical velocity has to be overcome. Let's consider a system with an excitation of momentum $\boldsymbol{p}$ and energy ϵ_p, the total energy in a reference frame that moves with a velocity $\boldsymbol{v}$ relative to the rest frame of the system can be expressed as

$$E(\boldsymbol{v}) = E + \epsilon_p - \boldsymbol{p} \cdot \boldsymbol{v} + \frac{1}{2} M v^2, \tag{2.85}$$

where M is the total mass of the system and E is the ground state energy of the rest frame. Comparing to the ground state of the system in the same moving frame,

$$E(\boldsymbol{v}) = E + \frac{1}{2} M v^2, \tag{2.86}$$

the energy required to create the excitation is $\epsilon_p - \boldsymbol{p} \cdot \boldsymbol{v}$. The minimum velocity that the system has to move with is hence

$$v_c = \min \left(\frac{\epsilon_p}{p} \right), \tag{2.87}$$

which is also known as the Landau critical velocity. ϵ_p / p is the phase velocity of the excitation. Above v_c, the total energy of the system has a non-negative loss. Below v_c, particles can be transported inside the fluid without dissipation, which is a critical feature of a superfluid. For a non-interacting Bose gas, the critical velocity is zero due to the absence of interparticle interactions. This makes an ideal Bose gas a poor description of superfluid He-4. On the other hand, exceeding v_c doesn't necessarily mean that a superfluid will turn into only normal fluid as the mutual interactions between excitations increase v_c. The lowest energy form of excitations are phonons and rotons.

Chapter 3

The numerical simulations

The non-linearity of the GPE makes solving it analytically very challenging. It is therefore justified to take a numerical approach, where the accuracy of the calculation depends on the spatial and temporal resolution. In the following we will introduce the linear approximation of the simulation for the time evolution of the wave function based on the time dependent GPE, the concept of phase imprinting and the exact computational implementation of the numerical methods that we have used.

3.1 The Fourier split operator method

There exist several numerical approaches for solving the time dependent GPE which are second-order nonlinear. We have chosen to use a pseudo-spectral Fourier split operator method to solve the GPE. Bauke and Keitel (2011) demonstrated that graphics processing units (GPUs) are capable of accelerating the fast Fourier transforms to an order higher than a central processing unit (CPU) implementation, because of this, we have chosen to use GPU to perform the computing.

For the split operator method, we start with the time dependent GPE for a 2D rotating condensate represented in the following form

$$-\frac{i}{\hbar}\frac{\partial}{\partial t}\Psi(\boldsymbol{r},t) = \hat{H}\Psi(\hat{r},t), \tag{3.1}$$

where $\hat{H} = \hat{K} + \hat{V} + \Omega_z \cdot \hat{L}_z$,

$$\hat{K} = \sum_{i=x,y} \frac{\hat{p}_i^2}{2m}, \quad \hat{p}_i = i\hbar\partial_i, \tag{3.2}$$

$$\hat{V} = \sum_{i=x,y} \frac{m\omega_i^2 r_i^2}{2} + g_{2D}\hat{n}, \tag{3.3}$$

$$\hat{L}_z = y\hat{p}_x - x\hat{p}_y = yi\hbar\partial_x - xi\hbar\partial_y. \tag{3.4}$$

Here $\hat{K}$ is an operator purely in momentum space and $\hat{V}$ is an operator purely in real space, while $\hat{L}$ is a product of operators from momentum space and operators from real space which commute ($[x, p_y] = [y, p_x] = 0$). The numerical solution of equation (3.1) has the form

$$\Psi(\boldsymbol{r}, t + dt) = \exp\Big(- \frac{i\hat{H}dt}{\hbar}\Big)\Psi(\boldsymbol{r}, t). \tag{3.5}$$

According to the Baker-Campbell-Hausdorff (BCH) formula (Shankar (1994)), non-commuting operators can be split in the following way

$$\begin{aligned}
\exp\Big(\frac{-i\hat{H}dt}{\hbar}\Big) &= \exp\Big(\frac{-idt}{\hbar}(\hat{K} + \hat{V} + \Omega \cdot \hat{L})\Big) \\
&= \exp\Big(\frac{-idt}{\hbar}(\hat{K} + \hat{V})\Big) \exp\Big(\frac{-idt}{\hbar}\Omega_z \hat{L}_z\Big) \exp\Big(\frac{-dt^2}{2\hbar^2}[\hat{K} + \hat{V}, \Omega_z \hat{L}_z]\Big) \\
&= \exp\Big(\frac{-idt}{\hbar}\hat{K}\Big) \exp\Big(\frac{-idt}{\hbar}\hat{V}\Big) \exp\Big(- \frac{idt}{\hbar}\Omega_z \cdot \hat{L}_z\Big) \\
&\exp\Big(\frac{-dt^2}{2\hbar^2}[\hat{K}, \hat{V}]/2\Big) \exp\Big(\frac{-dt^2}{2\hbar^2}[\hat{K} + \hat{V}, \Omega_z \hat{L}_z]\Big) \exp\big(\mathscr{O}(dt^3)\big).
\end{aligned} \tag{3.6}$$

When $dt \ll 1$, the second order and higher terms in equation (3.6) can be treated as unitary. By utilising the Strang splitting (symmetric splitting) from Gradinaru (2007), which makes this split operator method second-order globally accurate, we obtain

$$\psi(x, t+dt) \simeq \exp\Big(- \frac{idt}{\hbar}\Omega_z \cdot \hat{L}_z\Big) \exp\Big(\frac{-idt}{2\hbar}\hat{V}\Big) \exp\Big(\frac{-idt}{\hbar}\hat{K}\Big) \exp\Big(\frac{-idt}{2\hbar}\hat{V}\Big)\psi(x, t). \tag{3.7}$$

In the discrete Fourier transform, the momentum, p, is defined as

$$p_i(n) = \frac{2\pi n}{N\Delta r_i}, \qquad i = x, y, \tag{3.8}$$

where N is the size of the spatial resolution and Δr_i is the grid size in each spatial direction. Recall the Strang splitting in equation (3.7), the exact implementation we use is the following

$$\Psi_1(x, y, t + dt) = \exp(-i\hat{V}dt/2\hbar)\Psi(x, y, t), \tag{3.9}$$

$$\begin{aligned}
\Psi_2(x, y, t + dt) &= \exp(-i\hat{K}\frac{dt}{\hbar})\Psi_1(x, y, t + dt) \\
&= \mathscr{F}^{-1}_{x,y}\Big\{ \exp(-i\frac{\hat{p}_x^2}{2m}\frac{dt}{\hbar})\mathscr{F}_{p_x,y}\{\tilde{\Psi}(x, y, t + dt)\}\Big\} \\
&+ \mathscr{F}^{-1}_{x,y}\Big\{ \exp(-i\frac{\hat{p}_y^2}{2m}\frac{dt}{\hbar})\mathscr{F}_{x,p_y}\{\Psi_1(x, y, t + dt)\}\Big\},
\end{aligned} \tag{3.10}$$

$$\Psi_3(x, y, t + dt) = \exp(-i\hat{V}dt/2)\Psi_2(x, y, t + dt), \tag{3.11}$$

$$\begin{aligned}
\Psi(x, y, t + dt) &= \exp(\frac{it}{\hbar}\Omega_z \cdot \hat{L}_z)\Psi_3(x, y, t + dt) \\
&= \mathscr{F}^{-1}_{x,y}\Big\{ \exp(\frac{idt}{\hbar}\Omega_z \cdot y \cdot \hat{p}_x) \cdot \mathscr{F}_{p_x,y}\{\Psi(x, y)\}\Big\} \\
&- \mathscr{F}^{-1}_{x,y}\Big\{ \exp(\frac{idt}{\hbar}\Omega_z \cdot x \cdot \hat{p}_y) \cdot \mathscr{F}_{x,p_y}\{\Psi(x, y)\}\Big\},
\end{aligned} \tag{3.12}$$

where $\mathscr{F}$ stands for the fast Fourier transform (FFT) in 2D, while $\mathscr{F}_{x,p_y}$ means FFT in $y-$dimension ($y \to p_y$) and $\mathscr{F}_{p_x,y}$ means FFT in $x-$dimension ($x \to p_x$). $\mathscr{F}^{-1}$ denotes the inverse fast Fourier transform (iFFT), therefore $\mathscr{F}^{-1}_{x,y}$ means iFFT back to xy coordinates.

3.2 Generating the ground state of BECs containing vortices

The split operator method can be applied with imaginary time propagation to find the ground state of a condensate in the rotating frame. We start with a trial wave function, ψ_t, which we take to be the ground state wave function of the system in the Thomas–Fermi regime,

$$\psi_t(\boldsymbol{r}) = \theta\Big(\mu - V(\boldsymbol{r})\Big)\sqrt{\frac{\mu - V(\boldsymbol{r})}{N g_{2\mathrm{D}}}}, \tag{3.13}$$

where $V(\boldsymbol{r}) = \sum_{i=x,y,z} \frac{1}{2} m\omega_i^2 r_i^2$ is the trapping potential and θ is the Heaviside step function with $\theta(\geq 0) = 1$ and zero otherwise. In general, an arbitrary wave function can be expressed in terms of the eigenstates of that system

$$\psi_t = \sum_i C_i \psi_i, \tag{3.14}$$

where C_i is the amplitude of ψ_i. Applying this expression in the time-dependent Schrödinger equation, one gets

$$i\partial_t \psi_t = \hat{H} \sum_i C_i \psi_i = \sum_i C_i E_i \psi_i, \tag{3.15}$$

where E_i is the eigenenergy of ψ_i. The time evolution of the wavefunction is then

$$\psi_t(t) = \sum_i C_i e^{-iE_i t} \psi_i(t = 0). \tag{3.16}$$

Applying imaginary time, $t \to -it$, leads to an increasing exponential suppression of the states in higher orders. The amplitudes of all states are suppressed, including the true ground state, hence a renormalisation is needed after every evolution time-step in imaginary time. After a sufficient amount of imaginary time propagation, the true ground state of the system will be recovered. See figure 3.1 for the ground states of a BEC with a few vortices, where all the vortices are singly charged, namely a phase winding of 2π (in the counterclockwise direction).

3.3 Phase imprinting

Phase imprinting is a crucial technique for the purpose of our simulations. It allows one to manipulate the phase of a condensate to the desired form. This technique has been de-

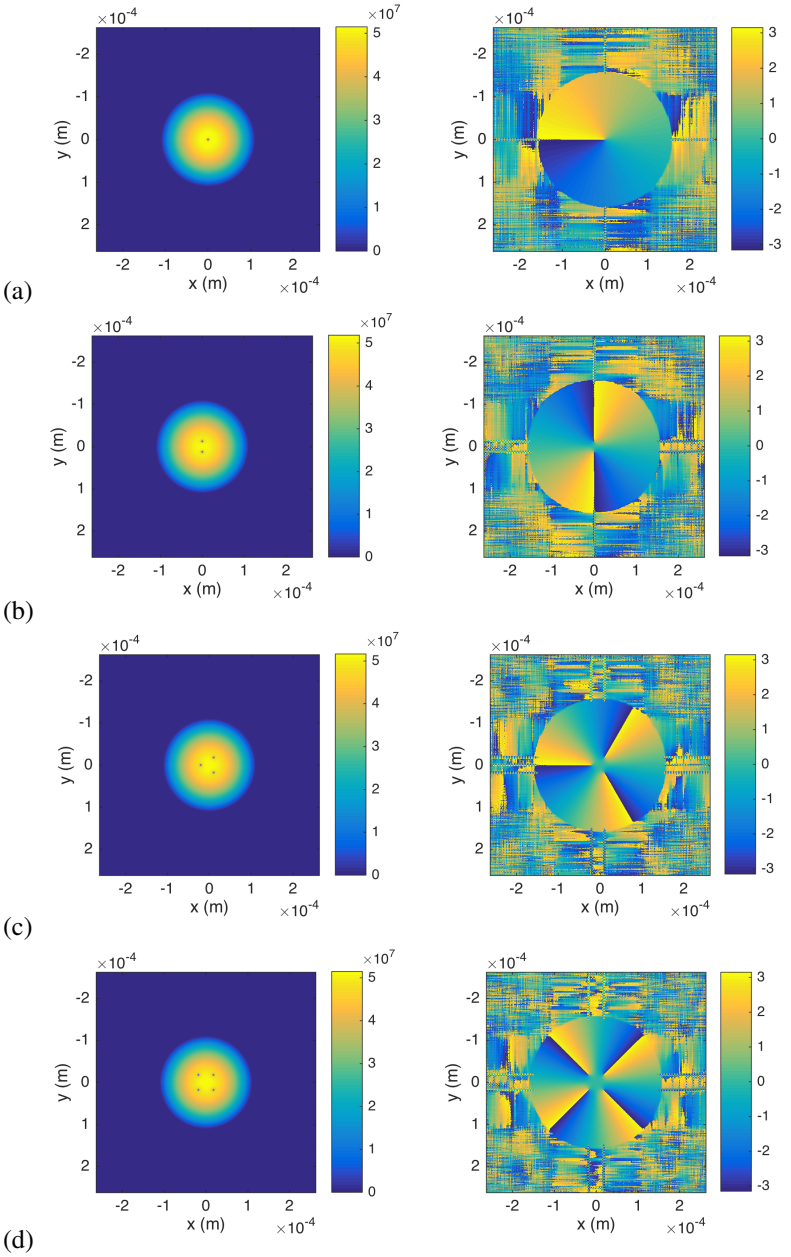

Figure 3.1: The ground state of BEC with respectively (a) one vortex, (b) two vortices, (c) three vortices and (d) four vortices. The plots in the left column are density plots. The plots in the right column depict the corresponding phasing winding of the BEC with different number of vortices.

scribed in great detail in Dobrek et al. (1999), where the authors demonstrated how to generate vortices in a BEC using this method numerically and potentially experimentally by using a far-off-resonant laser pulse. When one manually alters the phase of the condensate, the condensate density will adjust itself accordingly. Experimentally phase imprinting has been successfully applied to create quantum vortices (Möttönen et al. (2003), Brachmann et al. (2011)).

As discussed earlier, the nucleation of vortices in a rotating BEC is very sensitive to the rotation velocity. To generate the desired amount of vortices in the system, therefore requires knowledge of the corresponding rotation velocity that's needed. However, by phase imprinting the precise number of circulations in the BEC, the system will converge to the ground state with the right number of vortices at a rotation velocity which can be more roughly estimated.

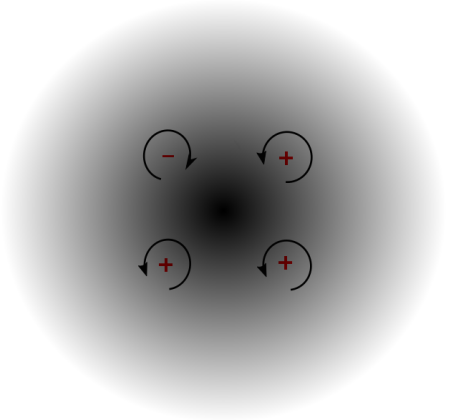

Figure 3.2: The configuration of 4 vortices in a 2D trapped atomic BEC, with 3 singly charged vortices with positive phase winding (+), and 1 singly charged vortex with negative phase winding (−).

Starting with the ground state of a BEC with a few singly charged vortices with positive phase winding (counterclockwise circulation), we can flip one of the vortices by phase imprinting a -4π circulation (clockwise circulation) within the healing length of the finite sized vortex. The resulting vortex configuration is shown in figure 3.2, which contains 3 vortices with positive phase winding and 1 antivortex with negative phase winding in the upper-left corner. This is an example of the initial states of our simulations, which we will explain in more detail later on.

3.4 GPU computing

With increasing spatial and temporal resolution of the simulation, the run time required for each simulation increases dramatically. A way of solving this is to introduce parallel computing, where the basic idea is to distribute the job among multiple processors, normally using CPUs (Central Processing Units). Common examples for this are OpenMP (Open Multi-Processing) and MPI (Message Passing Interface). The main difference is that OpenMP allows parallelism over local CPUs, while MPI enables a distribution over a cluster with in principle, an unlimited amount of CPUs available. The most simple and straight forward parallel computing problems are embarrassingly parallel. It means no exchange of message between different nodes, hence complete independence among nodes. Recently the use of GPUs (Graphic Processing Units) has become an important tool for massively parallel programming. GPUs are designed to handle large amount of pixels and 3D mathematical operations for image rendering. Mapping the computing operations effectively onto the hardware of GPUs significantly reduces the computing time. For the means of our simulations, the programming model CUDA has been used, which operates on a single instruction multiple thread (SIMT) architecture.

We apply a GPE solver named GPUE (O'Riordan et al. (2017)) using GPUs to evolve the 2D BEC wave function in the $xy-$plane. For our simulations we model 10^6 Rubidium-87 atoms confined within a 3D harmonic trapping potential with trapping frequencies $\boldsymbol{\omega} = (2\pi,\ 2\pi,\ 32\pi)\mathrm{Hz}$. The rotation rate of the trap is $\Omega_z = 0.3 \cdot 32\pi\mathrm{Hz}$. The interatomic interaction strength in the 2D BEC, g_{2D}, is equal to $6.67411 \times 10^{-40}\mathrm{m}^4 \cdot \mathrm{kg/s}^2$. We use a spatial grid of extent $(5.24 \times 10^{-4}\mathrm{m})^2$ in the $xy-$plane with 1024×1024 spatial grid points. A temporal resolution of $1 \times 10^{-5}\mathrm{s}$ is used for the real time evolution of the GPE. For vortex tracking, the wave function is sampled once per 1000 time steps, namely every $0.01\mathrm{s}$.

3.5 Vortex tracking

The location of vortices in the BEC is detected by looking at the phase winding in each cell. If the phase winding is an integer number of 2π, a vortex can potentially reside inside this cell. However, due to the low density around the edge of the trapped atomic cloud, the phase winding method gives too much noise and detects some vortices at and beyond the condensate edge which are not real vortices. Therefore we apply a mask that is slightly smaller than the radius of the atomic cloud, so that phases outside the mask are not considered. When we kill (annihilate) one vortex by phase imprinting an opposite charge on the vortex core, the energy of the vortices is transformed into phonons which propagate outwards from where the vortex used to be. In our system, no dissipation is considered, hence the phonons get reflected back from the edge of the condensate and create interference patterns. This contributes to small fluctuations over the entire cloud and also close to the centre of the vortex. Further verification of the existence of the vortices is thus needed.

This further verification is performed by looking at the atomic density in the cells that

were previously selected as they showed the phase-winding typical of a vortex. If the atomic density is equal to zero (numerically, this means that the density inside that cell is smaller than some predefined values), then we conclude that there's indeed a vortex residing inside this cell. Furthermore, in order to increase the precision of vortex positions identified to a finer resolution than the grid size, we apply a least-squares fit (as applied in Foster (2002)). In order to keep track of the vortices from one time frame to the next, an identifier is assigned to each vortex, as shown in figure 3.3.

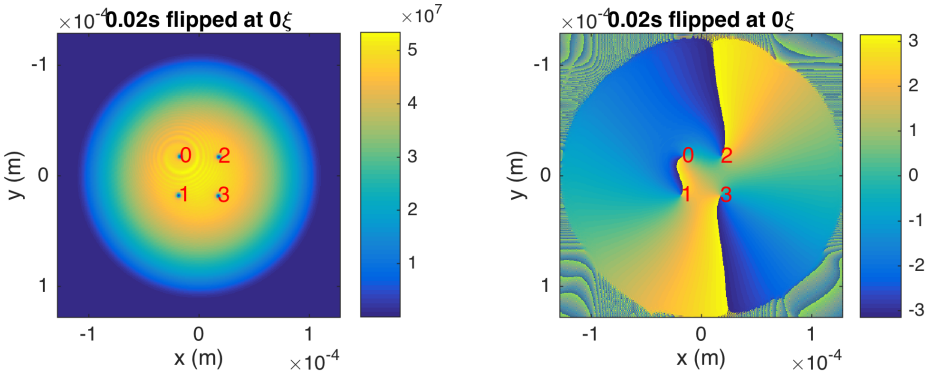

Figure 3.3: Vortex positions 0.2s after flipping the the upper left vortex (index 0). The numbers assigned to each vortex are their corresponding vortex identifier.

In this chapter we have discussed the numerical implementation of our simulations. This numerical implementation is developed by L. J. O'Riordan (O'Riordan and Busch (2016)) and the code source can be found online (O'Riordan et al. (2017)). The results and analyses of our numerical data, obtained using these GPU computing methods, will be presented in the following chapters.

Chapter 4

Chaos indicators

Classical chaos refers to chaotic dynamics in classical mechanics. Chaos theory from a mathematical point of view is the sensitivity of the behaviour of the dynamical system to the initial conditions. A well known example of this is the butterfly effect. A small change in the initial conditions results in a dramatic divergence of the long term behaviour of the system. Even though the system is deterministic, namely the dynamics of the system is fully determined by its initial conditions (there is no missing pieces in the puzzle), the outcome of a dynamical system subjected to a subtle difference in the initial conditions is unpredictable (Kellert (1993)). Besides the sensitivity of the initial conditions, a mixing in phase space should be present in the case of chaotic dynamics. Mixing means that two initially neighbouring orbits should wind around each other in a complicated way. In this chapter, two indicators of chaos are introduced. One of them is the classical Lyapunov exponent and the other is the small Alignment index which was first introduced in Skokos (2001). In ideal scenarios (that is infinite long time and infinite system size), chaotic dynamics are indicated by a positive Lyapunov exponent.

4.1 The Lyapunov exponent

The Lyapunov exponent is one of the most well-known and commonly used tools for determining chaos, however it is not necessarily the most efficient tool. Firstly, it relies highly on the exponential increase of the difference between near-by orbits which will ultimately be limited by the system size. Secondly, in the ideal definition of the Lyapunov exponent, time goes to infinity, which is not practically possible. For this reason, the value of the Lyapunov exponent can only be extrapolated. We are presenting a short definition of the Lyapunov exponent here (Wolf et al. (1985)).

We assume two initially neighbouring trajectories in a four-dimensional phase space

$$\boldsymbol{Z}_1(t) = (x_1(t), y_1(t), v_{x,1}(t), v_{y,1}(t)),$$
$$\boldsymbol{Z}(t) = (x(t), y(t), v_x(t), v_y(t)),$$

where $v_x(t) = \frac{dx}{dt}$ and $v_{x,1} = \frac{dx_1}{dt}$, with an initial separation

$$\delta \boldsymbol{Z}_0 = (\delta x_0, \delta y_0, \delta v_{x0}, \delta v_{y0}),$$

where $\delta x_0 = x_1(0) - x(0)$ and $\delta v_{x0} = v_x(0) - v_{x1}(0)$, ect. The separation between these two trajectories diverges with a rate (provided that linear approximation is applicable within $\delta \boldsymbol{Z}_0$),

$$\|\delta \boldsymbol{Z}(t)\| = e^{\lambda t} \|\delta \boldsymbol{Z}_0\|, \tag{4.1}$$

where $\lambda = \lambda(t)$ is the Lyapunov exponent and $\|\cdot\|$ is the Euclidean norm. Equivalently, the Lyapunov exponent is defined as

$$\lambda(t) = \lim_{\delta \boldsymbol{Z}_0 \to 0} \frac{1}{t} \ln \frac{\|\delta \boldsymbol{Z}(t)\|}{\|\delta \boldsymbol{Z}_0\|}, \tag{4.2}$$

and the Lyapunov characteristic exponent (LCE) is

$$\lambda_C = \lim_{t \to \infty} \lambda(t). \tag{4.3}$$

A positive LCE in a Lyapunov exponent spectrum indicates a chaotic system, and the value of the LCE indicates the strength of chaos. Larger LCEs correspond to strong chaos and smaller LCEs correspond to weak chaos.

Alternatively, one can also define a one-dimensional Lyapunov exponent, λ_i. For orbits in n-dimensional phase space,

$$\lambda_i = \lim_{t \to \infty} \lim_{\delta z \to 0} \frac{1}{t} \ln \frac{Z_i(t)}{Z_i(0)}, \qquad i = 1, \cdots, n. \tag{4.4}$$

λ_i is arranged in a decreasing order. λ_1 is called the maximal Lyapunov exponent, whose value is also often used as an indicator of chaos. For the means of this project, we have calculated λ_x, which is the Lyapunov exponent considering only $Z_x = (x, v_x)$, and λ_y, which is the Lyapunov exponent over $Z_y = (y, v_y)$ and λ_r, which is the Lyapunov exponent over all degrees of freedom, namely $\boldsymbol{Z} = (x, y, v_x, v_y)$.

As argued in the beginning of this section, in practice, the numerical Lyapunov exponents are all calculated during finite time intervals. These Lyapunov exponents are often referred to as a finite Lyapunov exponent. Vallejo and Sanjuán (2013) have applied the finite Lyapunov exponent on computing the hyperbolicity index of two coupled Rössler oscillators. It's been argued that the choice of the finite time interval is dependent on the convergence rate of the Lyapunov exponent. In particular for our system, the choice of our time invterval should be comparable with an experimentally realisable lifetime of BECs.

4.2 The smaller alignment index (SALI)

The Smaller Alignment index (SALI) is a simple chaos indicator. Its definition is expressed as (Skokos (2001) and Skokos et al. (2004)),

$$\text{SALI}(t) = \min\left\{\|\boldsymbol{\nu}_1(t) + \boldsymbol{\nu}_2(t)\|, \|\boldsymbol{\nu}_1(t) - \boldsymbol{\nu}_2(t)\|\right\} = \min\left\{\|\text{sum}\|, \|\text{sub}\|\right\}, \tag{4.5}$$

where $\boldsymbol{\nu}_1(t)$ and $\boldsymbol{\nu}_2(t)$ are the normalised deviation vectors of two pairs of close-by orbits. In other words,

$$\boldsymbol{\nu}_1(t) = \frac{\delta \boldsymbol{z}_1(t)}{\|\delta \boldsymbol{z}_1(t)\|},$$
$$\boldsymbol{\nu}_2(t) = \frac{\delta \boldsymbol{z}_2(t)}{\|\delta \boldsymbol{z}_2(t)\|}.$$

See figure 4.1 for an illustration of how deviation vectors are defined based on three close-by orbits. In principle, $\text{SALI}(t) \in [0, \sqrt{2}]$, where $\text{SALI} = 0$ means that $\boldsymbol{\nu}_1 = \pm\boldsymbol{\nu}_2$ and

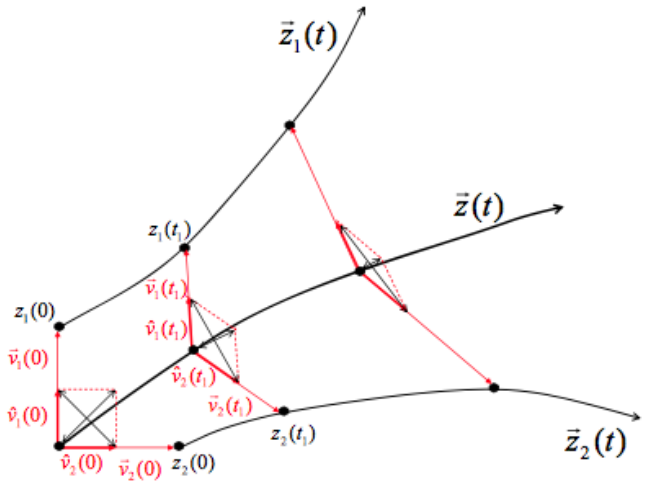

Figure 4.1: An illustration of the deviation vectors, $\vec{\nu_1}(t)$ and $\vec{\nu_2}(t)$, of three close-by orbits, $\vec{z}_1(t)$, $\vec{z}_2(t)$ and $\vec{z}(t)$ as a reference orbit. Figure is reprinted from Benitez et al. (2015).

$\text{SALI} = \sqrt{2}$ means that $\boldsymbol{\nu}_1 \perp \boldsymbol{\nu}_2$. If two orbits are chaotic, $\boldsymbol{\nu}_1$ and $\boldsymbol{\nu}_2$ will align arbitrarily relative to each other. This leads to an overall SALI value that tends towards zero for chaotic behaviours (aka. the two deviation vectors tend to coincide or become opposite) in a $2n$-dimensional phase space with $n \geq 2$ (Voglis et al. (1999)). "This due to the fact that the directions of the two deviations vectors tends to coincide with the direction of the most unstable nearby manifold" (Skokos et al. (2002)). In numerical studies, it is common to set a threshold value for SALI under which the orbits are defined as chaotic (Antonopoulos et al. (2010)).

A study on the dynamics of three point vortices (two positvely and one negatively charged) has been performed with the help of SALI as a chaos detection tool (Kyriakopoulos et al. (2014)). In contrast to our system which starts from the ground state of BECs, various vortex configurations in phase space with three vortices has been investigated. Within the configuration space, there are divisions between regular and chaotic regions, that is, some initial vortex configurations lead to regular dynamics and others lead to chaotic dynamics. The threshold value under which the dynamics is defined as chaotic, that has been

set in this article to (10^{-12}) is not realistic for our numerical data due to the limitation of the spatial resolution in our system.

These two chaos indicators, SALI and the Lyapunov exponent, that have been discussed in this chapter, will be applied to our numerical results later on in this thesis. We will use these chaos indicators to verify or disprove the chaotic features of trajectories of a few vortex systems in a rotating BEC.

Chapter 5

Regular quantum vortex dynamics in a 2D BEC

The existence of quantum vortices provides direct evidence for superfluidity. Vortices located at the centre of a harmonically trapped BEC will contribute an angular momentum of order $\hbar$ proportional to the charge of the vortex. The angular momentum contribution decreases with increasing distance between the vortex cores and increasing distance from the centre of the condensate (Chevy et al. (2000)). Due to the robustness of quantum vortices, they can be treated as classical particles and their interactions also resemble interactions between classical particles. Our work has mainly been focusing on few vortex systems. In this chapter we will discuss non-chaotic quantum dynamics of systems consisting of one, two and four vortices respectively.

5.1 Dynamics of a single vortex in a BEC

The ground state of a BEC with a single vortex is very simple and straight forward from the perspective of dynamics. In rotating BECs, this single vortex is created along the rotation axis. Figure 5.1 shows a slice through the centre of the density profile of the BEC, together with a contour plot of the density, which shows an isotropic density drop radially outwards from the centre of the condensate.

With real time propagation, this central vortex remains stationary even after applying perturbations to it. We have in particular flipped the direction of rotation of the single central vortex in our simulation by phase imprinting a 4π phase with a direction opposite to that of the vortex's circulation (counterclockwise). Phonons are created due to the annihilation of the original vortex, but the flipped vortex (antivortex) remains stationary. See figure 5.2 for the density and phase plot of a single flipped central vortex (an antivortex) with a negative phase winding (clockwise circulation). The blue dip in the

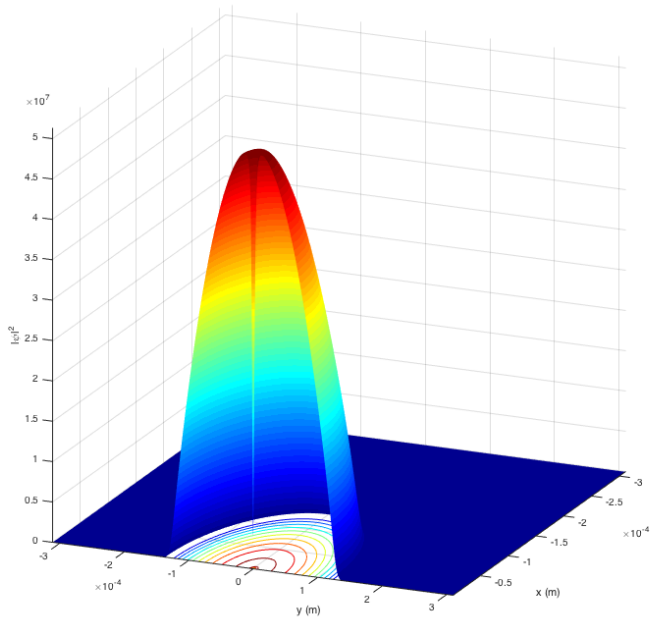

Figure 5.1: A slice through the density profile, $|\psi|^2$, of a BEC with one singly charged vortex at the condensate center. A contour plot of the xy-plane of the BEC density profile is also plotted.

centre indicates a density drop inside a vortex which is also an indication of the size of the vortex,$\xi \simeq 5.11 \times 10^{-6}\mathrm{m}$, where ξ denotes the healing length.

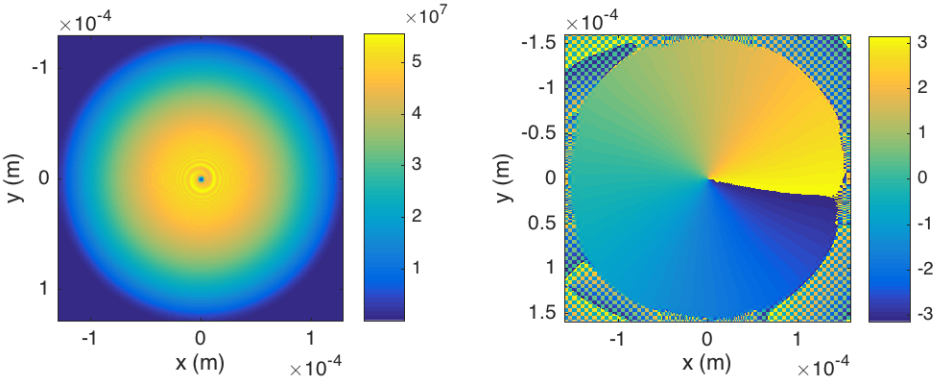

Figure 5.2: To the left: The density plot of BEC $0.01\mathrm{s}$ after flipping the central vortex right on the vortex core. To the right: The phase plot of BEC $0.01\mathrm{s}$ after flipping the central vortex right on the vortex core.

In O'Riordan and Busch (2016), the author employed the same phase imprinting technique to flip a single central vortex in a similar BEC system, generated by the same computing method (O'Riordan et al. (2017)). They found that phase imprinting within a distance equal to twice the healing length can successfully annihilate and flip the pre-existing vortex.

5.2 Dynamics of two vortices in a BEC

The location of two singly charged vortices (counterclockwise phase winding in the context of this work) in a BEC is shown in figure 3.1 (b). In the absence of any perturbation, the two vortices rotate around each other in a circular orbit and the relative distance between them in the laboratory frame is preserved. Flipping one of the vortices exerts a rotation that resembles the gravitational two-body problem Keeton (2014). The additional phonon modes in the condensate created after annihilating the original vortex don't effect the vortex trajectories. See figure 5.3 for the trajectory of the two vortices over a time of $50\mathrm{s}$ after vortex flipping. In figure 5.3, both the raw vortex trajectory (obtained directly by our vortex tracking algorithm) and the smooth vortex trajectory (obtained by applying a running average over the raw data) are shown. The plots show that the smoothed trajectories still follow the original trajectories very well, except are absent of the small oscillations which are especially evident in the antivortex trajectory. Hereafter we base most of our calculations on the smoothed vortex trajectories, with the exception of the histograms of vortex position that we are presenting next. It is important to remark that all quantities are measured in the co-rotating frame.

Alternatively, we can represent the vortex trajectories with histograms of their position.

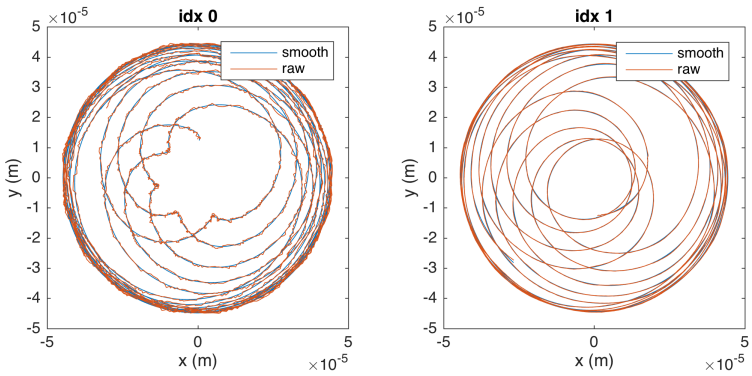

Figure 5.3: A comparison between the trajectories of two vortices (idx 0 is the antivortex and idx 1 is the vortex) in the co-rotating frame before ('raw') and after ('smooth') applying smooth function in the co-rotating frame. These are trajectories following the flipping right on the vortex core of vortex with idx 0.

We divide the 2D box of size $(5.26 \times 10^{-4}\mathrm{m})^2$ into a 256×256 grid. The number that is associated with each grid cell of the histogram counts how many times a vortex crosses that grid cell during a chosen time period. Tracking the vortex trajectories during $t = 50\mathrm{s}$ with a temporal step size of $\delta t = 10\mathrm{ms}$ gives the histogram shown in figure 5.4. The trajectories of the two vortices in both real space and momentum space look ordered. Both vortices have a tendency to move to the outer region of the condensate in order to minimise the vortex energies. From histograms, it is easy to tell where each vortex has spent most of its time. The histograms in figure 5.4 show that some time after vortex flipping, both the vortex and the antivortex move in regular circular orbits.

Although the trajectories seem to be regular, it is important to check how this depends on the location of the vortex which is flipped by phase imprinting. We are comparing the trajectories of individual vortices when one of the two vortices is flipped at an offset of 0.1ξ and 0.08ξ, where ξ is the healing length ($\xi = 5.11 \times 10^{-6}\mathrm{m}$). The difference between these two sets of trajectories, $(\Delta x(t), \Delta y(t)) = (x_2(t) - x_1(t), y_2(t) - y_1(t))$, where $(x_1(t), y_1(t))$ and $(x_2(t), y_2(t))$ are the positions of a vortex which is flipped at respectively 0.08ξ and 0.1ξ away from its original position, is shown in figure 5.6. The blue line in the figure is the antivortex and the red line is the vortex. It appears that the separation between the initial close-by orbits of the vortex behaves in an ordered way, while the antivortex has a more irregular motion. In order to check whether or not the motion of antivortex is chaotic or not, we calculate the Lyapunov exponent spectrum of the antivortex, as well as the vortex. This result is shown in figure 5.7. The Lyapunov exponent of the antivortex ('idx 0') converges to zero at around $10\mathrm{s}$ after the vortex flipping occurs. The Lypunov exponent of the vortex on the other hand is positive during this time period, however it decrease relatively fast towards zero.

The dynamics between the vortex and antivortex is investigated by calculating the relative distance between them with respect to time. This is shown in figure 5.5, where

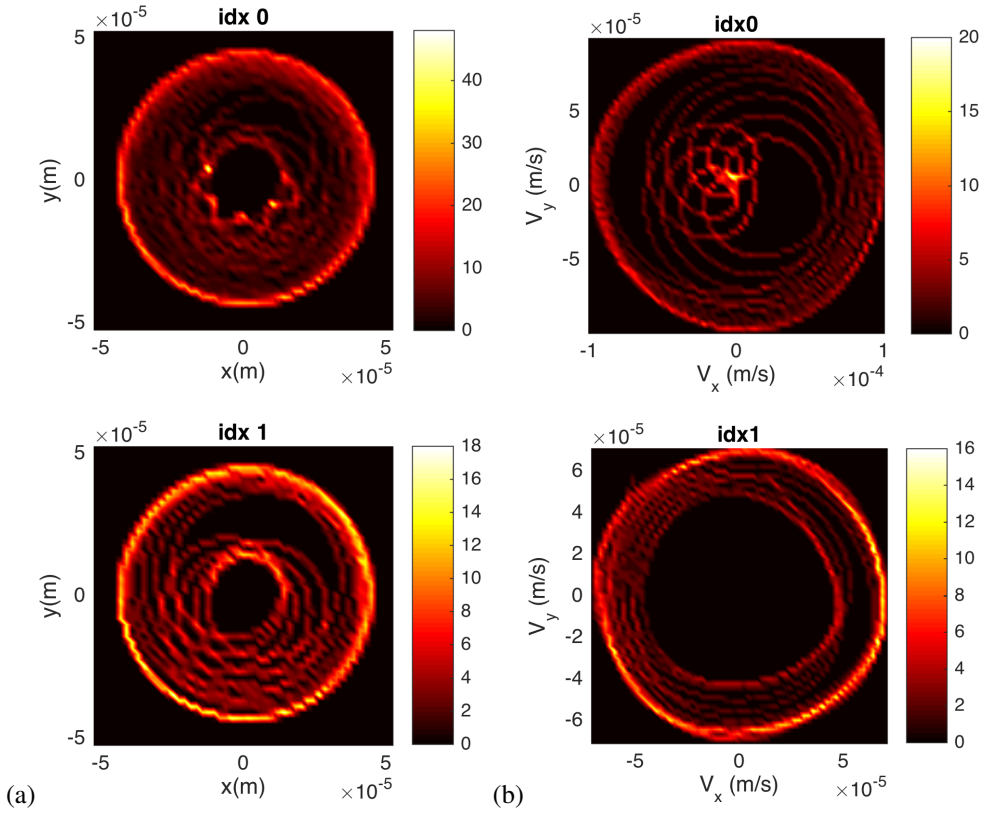

Figure 5.4: Histograms of the trajectories over a time-period of 50s of one antivortex ('idx 0') and one vortex ('idx 1') in the co-rotating frame in a BEC. The antivortex is created by flipping one of the two vortices in the generated BEC ground state, right on the vortex core. (a) depicts the histogram that represents the vortex trajectories in real space. (b) is the corresponding histogram of the velocity of each vortex during the 50s of evolution.

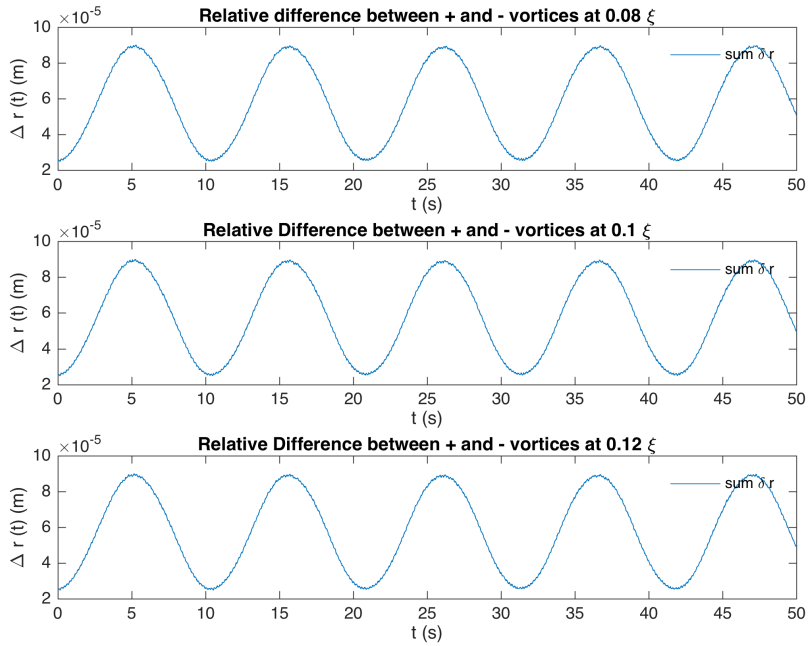

Figure 5.5: The relative distance between the vortex and the antivortex, sum δr, over a time-period of 50s shown for three sets of trajectories, where the vortex is flipped at respectively 0.08ξ (upper plot), 0.1ξ (middle plot) and 0.12ξ (lower plot) from the original vortex core position.

three sets of simulations are shown corresponding to vortex flipping located at 0.08ξ and 0.1ξ and 0.12ξ away from the original vortex core position. The relative distance, $\delta r = \sqrt{\delta x^2 + \delta y^2}$, where $(\delta x, \delta y)$ is the relative separation between the vortex and the antivortex for the same simulation, presents a very regular oscillation, regardless of the flipping distance from the original vortex. This oscillation resembles the gravitational two-body problem that has been used to describe the orbits between two celestial bodies with similar mass (Keeton (2014)).

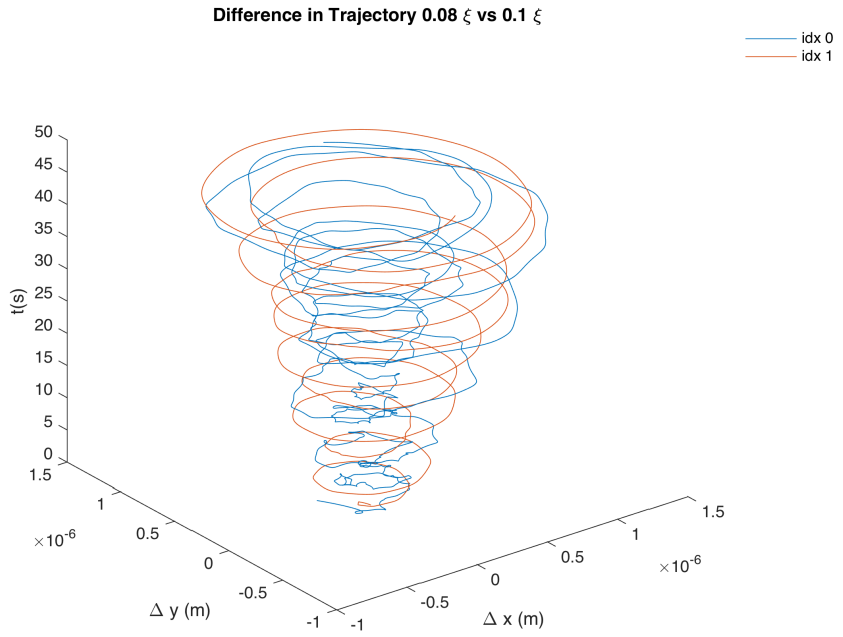

Figure 5.6: The separation between initially close-by orbits, when one of the two vortices is flipped at 0.1ξ and 0.08ξ away from the original vortex core. idx 0 denotes the antivortex and idx 1 the unflipped vortex.

5.3 Regular dynamics of four vortices in a BEC

When the system consists of a larger number of vortices, the vortex dynamics can be more complex. In the previous section, even though we perturbed the system by flipping a vortex, we did not cause the vortices to show chaotic dynamics. As we will show in next chapter, increasing the number of vortices in the system successfully complicates the dynamics sufficiently to detect chaotic trajectories. Our aim in this section is to create ordered dynamics for identical numbers of vortices as this will be used as a reference in

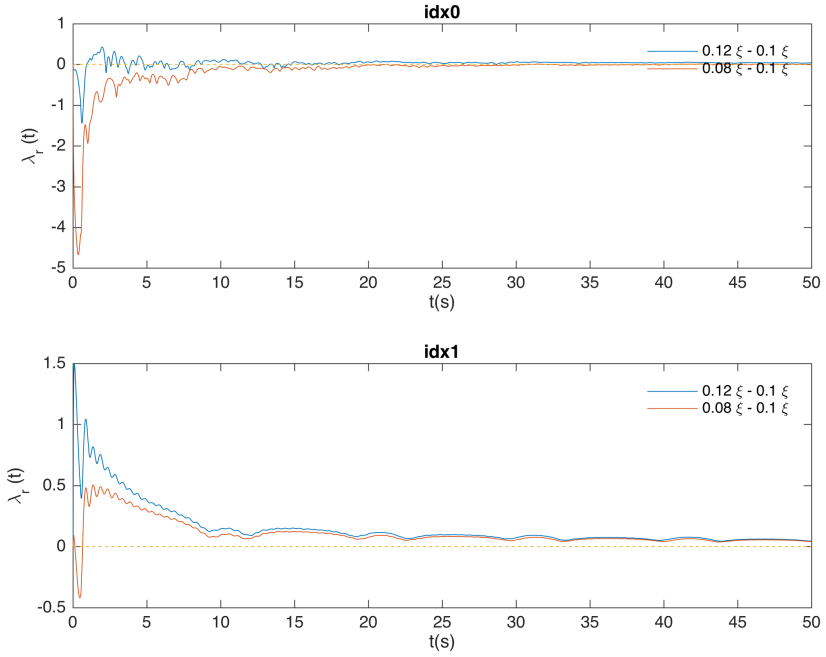

Figure 5.7: The Lyapunov exponent spectrum of an antivortex,'idx 0', and a vortex, 'idx 1', in the BEC in a time period of 50s. Two Lyapunov expnonent series for each vortex calculated based on three initially neighbouring orbit created after vortex flipping at 0.12ξ (blue) and 0.08ξ (red) and 0.1ξ (the reference orbit).

the next chapter. We focus on using four vortices with a diferent perturbation to initiate the dynamics. Compared to flipping the direction of rotation of a vortex, we need a more subtle perturbation to ensure regular vortex dynamics.

Instead of a -4π phase imprinting (vortex flipping), we are applying phase imprinting of -2π to annihilate a vortex and after a few steps in real time evolution, phase imprint 2π to create a new vortex near the original one with the same direction of rotation. Using this procedure, we can finely tune the location of the new vortex using a similar method to that we have applied to get an antivortex in the previous section. The induced motion of the vortices when we create a new vortex exactly where the annihilated one was is shown in figure 5.8.

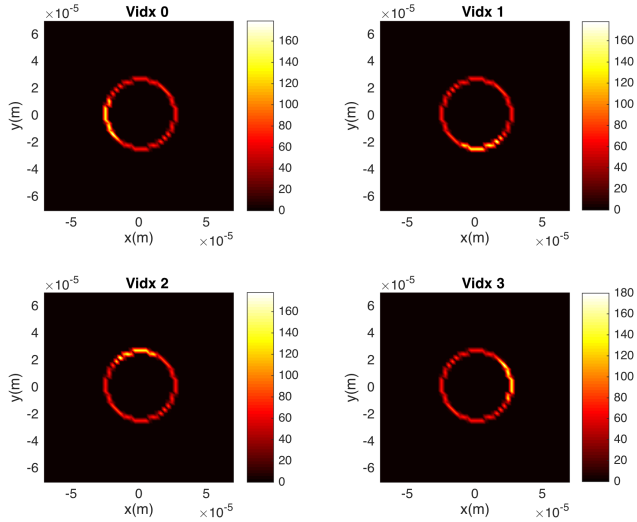

Figure 5.8: The 2D histograms of the position of individual vortices in position space for a system of four vortices , plotted over a total time evolution of 50s with step size of 0.01s. The vortex with index 0 has been annihilated and re-imprinted exactly on the original vortex core.

The trajectories of the four vortices with one of them re-imprinted slightly off-set from the original vortex postion is shown figure 5.9. This figure indicates that the four vortices stay in a square lattice and rotate collectively in the co-rotating frame of the BEC. The direction of rotation is dependent on where the new vortex is created, as we can observe from figure 5.9. In this figure, the COM (centre of mass) trajectories are also shown. This quantity depicts the vortices as one single parameter and is to be introduced in the next chapter. The separation in time between two close-by orbits, when we have re-imprinted a vortex at 0ξ and 0.1ξ away from the original vortex position, is shown in figure 5.10. Figure 5.11 shows the relative distances between the re-imprinted vortex and the 3 other vortices, given by δr_{i-0} which denotes the relative distance between the re-imprinted vor-

tex, 'idx0', and the unperturbed vortex, 'idx i', where $i = 1,\ 2,\ 3$. The behaviour of the relative distances in time further confirms our statement that the four vortices rotate in the co-rotating frame with a preserved lattice structure.

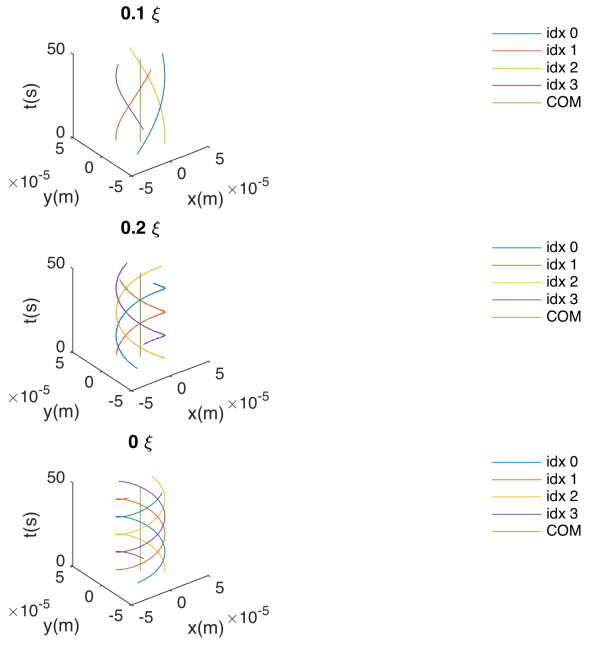

Figure 5.9: The trajectories of four vortices in the co-rotating frame over a time period of 50s, where the position of one of the vortices is slightly dislocated by re-imprinting a new vortex at 0.1ξ (upper plot), 0.2ξ (middle plot) and 0ξ (lower plot) relative to the position of the original vortex that was annihilated. 'idx 0' refers to the re-imprinted vortex, while 'idx 1', 'idx 2' and 'idx 3' are the unperturbed vortices. The COM trajectories of the four vortices are also shown.

In this chapter we have investigated vortex dynamics in BECs by studying the trajectories of one vortex and one antivortex created from the ground state of a BEC containing two co-rotating vortices. We have also looked at the trajectories of four vortices in a BEC, when the location of one of the vortices is slightly off-set by annihilating one of the four vortices orignially generated in the ground state and creating a new vortex at a slightly different position. The dynamics between a vortex and an antivortex have been confirmed to be regular by calculating the Lyapuov exponent spectrum, even though the separation between the trajectories of the antivortex has shown some irregularity (see figure 5.6). Slightly dislocating the position of one of the four vortices in the generated BEC ground state causes all four vortices to rotate collectively in the co-rotating frame with a preserved lattice structure. In next chapter, we will look into the dynamics of more than two vortices after applying vortex flipping in search of more complex dynamics.

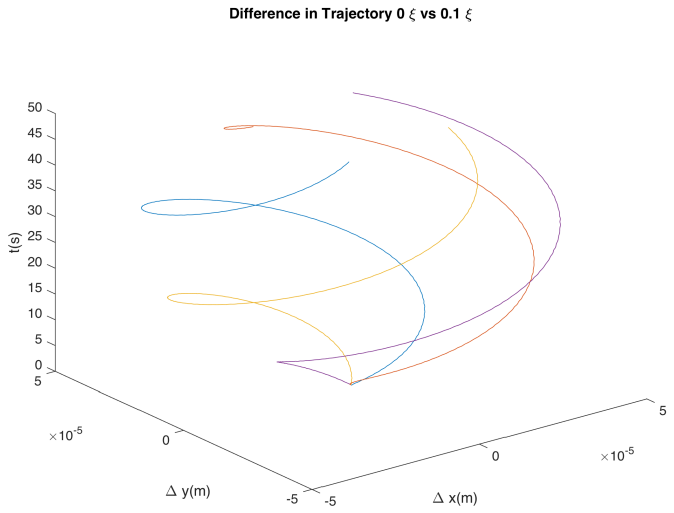

Figure 5.10: The separation of individual vortex trajectories after phase imprinting a new vortex at 0ξ and 0.1ξ away from the original vortex location in the co-rotating frame of the BEC. The blue line denotes the re-imprinted vortex and other coloured lines denote the 3 other vortices.

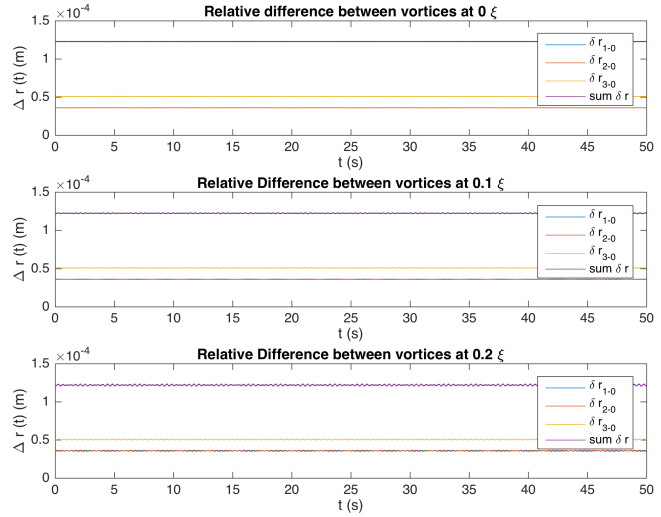

Figure 5.11: The relative distance between the re-imprinted vortex and the 3 unperturbed vortices, denoted as $\delta r_{1-0}, \delta r_{2-0}$ and δr_{3-0}, in the co-rotating frame of the BEC, shown for three sets of simulations where the phase imprinting location is respectively 0ξ (upper plot), 0.1ξ (middle plot) and 0.2ξ (lower plot) from the original vortex core position. The sum of these relative distances is also presented as sum δr.

Chapter 6

Chaotic quantum vortex dynamics in a BEC

Many previous studies have looked into chaotic dynamics of few vortex systems, both analytically and numerically (e.g.Murty and Rao (1970), Aref (1983), Speetjens et al. (2014)). Most of these studies have been based on the point vortex model, which ignores the internal structure of the vortices (Wisniacki et al. (2007), Fangohr et al. (2001), Haldane and Wu (1985)). We are, on the other hand, simulating physical vortices with finite sizes. Although they start from different configurations, chaotic dynamics have been observed in a system of three and four point vortices. Inspired by this, in this chapter we will be focusing on a BEC system containing three and four vortices respectively, with one of the vortices flipped. We finely adjust the flipping distance from the original vortex core position and keep track of the resulting vortex trajectories to create a sequence of initially near-by orbits. This allows us to apply the chaos indicators on the resulting trajectories and to verify or disprove whether the vortex trajectories induced by vortex flipping are chaotic.

6.1 Chaotic dynamics of three vortices in a BEC

We consider systems of three vortices in order to search for more complicated dynamics between vortices. In A. T. Conlisk and Elliott (1989), the authors have studied the vortex motion among three invscid equally charged point vortices above a flat wall. During this study, they have fixed the location of two vortices while they alter the position of the third one along the line perpendicularly intersecting the middle of the line segment between the two fixed vortices. It has been shown that as the the third vortex moves closer to the other two vortices, the vortex motions transit from regular to chaotic, which is verified with the Lyapunov exponent spectrum (among other tools). It's reasonable to assume that we can expect some chaotic behaviour in our system of three vortices, which is more complex due to the inhomogeneity of the atomic density of a harmonically trapped BEC and the finite

size of quantum vortices, where the healing length gives the typical vortex radius $\xi > 0$.

In a similar manner to that applied in the previous chapter, we are flipping (reversing the circulation) of one of the three vortices in the BEC as shown in 3.1. The first sign of chaotic behaviour, after flipping a single vortex in a three-vortex system exactly on the original vortex core position and considering the resulting trajectories in the co-rotating frame, comes from the disordered nature of the vortex trajectories themselves as shown in figure 6.1. See figure 6.2 for a histogram of the vortex trajectories in the co-rotating frame

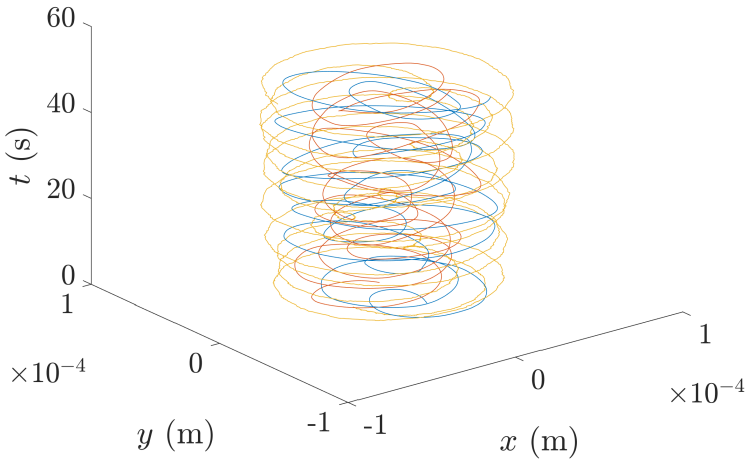

Figure 6.1: The vortex trajectories of individual vortices in the co-rotating frame, after flipping one vortex right on the original vortex core position, plotted over an evolution time of 50s. The blue line shows the trajectory of the antivortex. The red and yellow line are respectively trajectories of the two other unperturbed vortices.

over 50s of evolution time after the vortex flipping. This histogram shows how frequently vortices cross each grid cell. All three vortices seem to travel around and across all the regions inside the condensate. In particular, the antivortex ('idx 0') moves faster and more irregularly. Furthermore, we also compare two sets of vortex trajectories with a slight difference in the initial position of the flipped vortex, that is we consider an initial position of the flipped vortex 0.2ξ away and 0ξ (same position) away from the original vortex site before flipping. The difference between the two sets of trajectories is shown in figure 6.3. Drastic divergences between two initially close-by vortex trajectories are observed. It is around $t = 10$s that the divergence in trajectories starts to occur. This will be looked at in more detail in the next section.

As well as looking at the individual trajectories, we are curious about how the entire

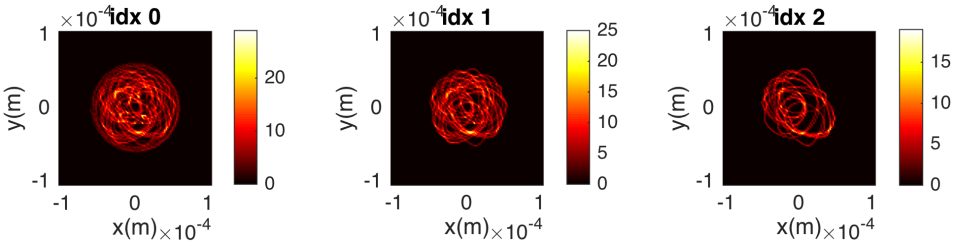

Figure 6.2: The histogram of vortex trajectories in the co-rotating frame where idx 0 is the antivortex and idx 1 and idx 2 are the two vortices, respectively. The histogram is plotted over a time period of 50s after vortex flipping right on the vortex core.

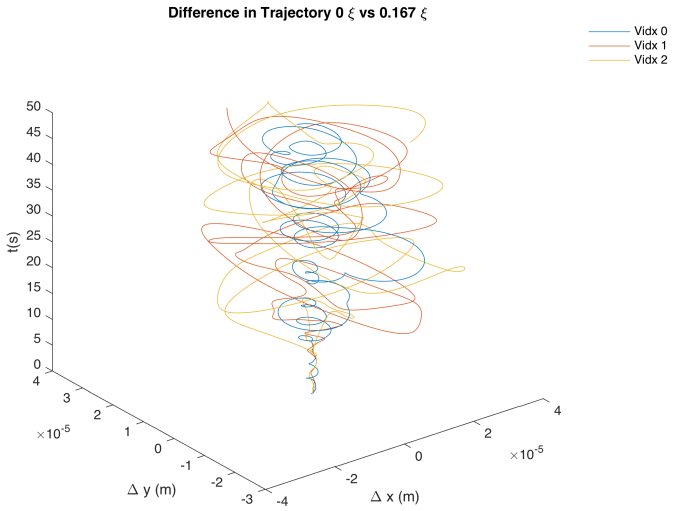

Figure 6.3: The time evolution of the difference between trajectories of the individual vortices, where the vortex with index 0 (idx 0) has been flipped initially at 0ξ and 0.1ξ away from the original vortex core. 'idx' denotes the vortex index of the 3 votices in the system.

system evolves with time. We define the following parameters

$$\boldsymbol{R}_{\text{COC}} = \frac{1}{n} \sum_{i\in[1,n]} \boldsymbol{r}_i - \boldsymbol{r}_0, \tag{6.1}$$

$$\boldsymbol{V}_{\text{COC}} = \frac{1}{n} \sum_{i\in[1,n]} \boldsymbol{v}_i - \boldsymbol{v}_0, \tag{6.2}$$

$$\boldsymbol{R}_{\text{COM}} = \frac{1}{n} \sum_{i\in[0,n]} \boldsymbol{r}_i, \tag{6.3}$$

$$\boldsymbol{V}_{\text{COM}} = \frac{1}{n} \sum_{i\in[0,n]} \boldsymbol{v}_i, \tag{6.4}$$

where the subscripts denote the index corresponding to the n vortices in the system, where the vortex with index 0 is the antivortex. COC and COM stand respectively for the centre of charge and centre of mass. The COC takes into account the sign of the charge of the vortices, while the COM treats vortices and antivortices equally. The COM and COC trajectories after flipping at the vortex core (0ξ) are shown in figure 6.4. Both trajectories present some irregular rotations in the co-rotating frame inside the condensate. The difference between the two sets of COC and COM trajectories with vortex flipping at 0.2ξ and 0ξ are shown in figure 6.5. The difference between the near-by trajectories of the entire system also diverges in time, however the abrupt divergence that is observed by looking at the difference between near-by single vortex trajectories is not very pronounced here.

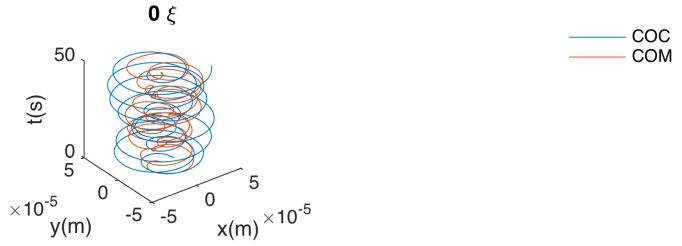

Figure 6.4: The COC (blue line) and COM (red line) trajectories of a system of 2 vortices and one antivortex in the co-rotating frame with vortex flipping right on the vortex core (0 ξ away from the original vortex position).

Besides the divergence of separation between initially near-by trajectories, an interwinding of two orbits occurs in phase space. Since we are treating vortices as classical particles, the momentum of vortices, according to the classical definition, is the product between the velocity of a vortex and its mass. The real mass of a quantum vortex is not a very relevant quantity, since a quantum vortex is not a particle. Instead of a momentum, we are using the vortex velocity obtained as the time derivative of the vortex position, $V_x = \Delta x/\Delta t, V_y = \Delta y/\Delta t$, where Δx and Δy are the differences in vortex position in the $x-$direction and the $y-$direction during a time Δt. In figure 6.6, the COC and COM trajectories of 2 vortices and one antivortex in the co-rotating frame during a time period of 50s, when the antivortex is created at 0.08ξ and 0.1ξ from the original vortex

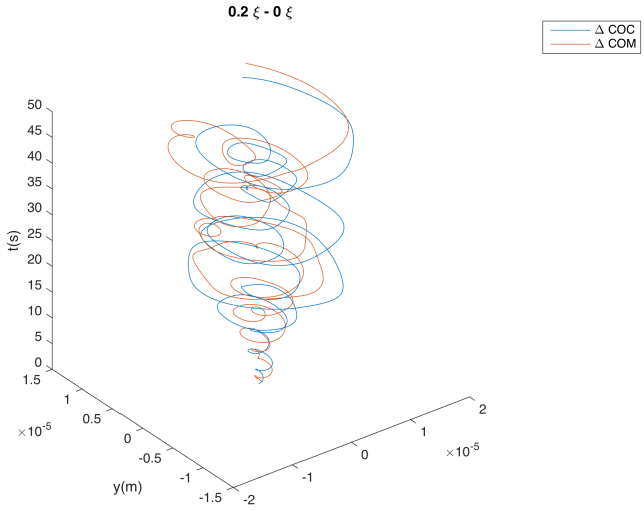

Figure 6.5: The difference between COC (red) and COM (blue) trajectories of a system composed of 2 vortices and one antivortex, after vortex flipping at 0.2ξ and 0ξ respectively, during a time period of 50s.

site, are shown in phase space, (x, V_x) and (y, V_y). These trajectories from the two sets of simulations mix with each other. This mixing of trajetories is another sign of chaotic behaviour.

All the above observations have shown signs of a chaotic behaviour. By calculating the spectrum of the Lyapunov exponent, some solid evidence of chaos may be gained. The corresponding Lyapunov spectrum is shown in figure 6.7. The Lyapunov spectrum of the antivortex (idx 0) seems to approach zero. The average of λ over a time range of $[45\text{s}, 50\text{s}]$ is $\simeq 0.01$. The Lyapunov spectrum of the other two vortices seems to converge to a larger average value of λ which is $\lambda \simeq 0.05$, which is an indication of stronger chaos. The stronger chaos of the two unperturbed vortices can also been observed from the irregularity of the trajectories of these vortices. The Lyapunov spectrum calculated from the COM trajectory of two vortices and one antivortex is shown in figure 6.8. This spectrum has a stronger oscillation than the spectrums for the individual vortices. There are also dips in the spectrum which go below zero. It's worth mentioning that the average λ for $t \in [45\text{s}, 50\text{s}]$ is positive.

The relative distance between the antivortex and the other two vortices with vortex flipping at 0ξ, 0.1ξ and 0.2ξ away from the original vortex core are illustrated in figure 6.9. In a system with three vortices, initially (before flipping) the three vortices are located at each corner of a regular triangle. The respective relative distances between the two vortices and the antivortex are equal. The relative distances show strongly entangled oscillations

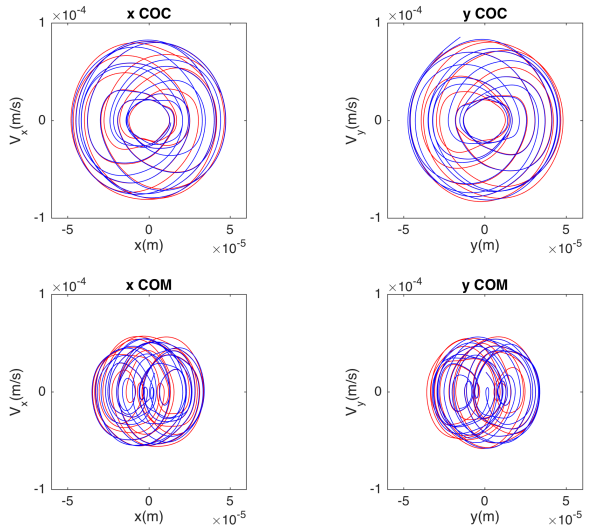

Figure 6.6: The orbits of $R_{\mathrm{COC}}, V_{\mathrm{COC}}$ of two vortices and one antivortex in phase space. The red line indicates the orbit of the sytem where the vortex flipping takes place at 0.1ξ and the blue line depicts the system's orbit with flipping at 0.08ξ.

with time. These oscillations are identical despite the flipping distance.

6.2 Chaotic dynamics of four vortices in a BEC

BECs with three vortices with one of them flipped have already shown some signs of chaotic dynamics and we have been able to confirm this quantitatively by calculating the Lyapunov exponent spectrum in the previous section. The antivortex, however, shows a very weak sign of chaos both according to the trajectories and the respective Lyapunov exponent spectrum. In this section, we will be looking at at a system of four vortices in our BEC. The corresponding ground state is shown in figure 3.1 and the configuration after flipping one of the four vortices is shown in figure 3.3, where the numbering indicates the vortex index and index '0' denotes the antivortex.

The histogram plot of the occurrence of each vortex inside each grid cell during a time period of $50\mathrm{s}$ sampled every $10\mathrm{ms}$ is shown in figure 6.10. Here the resolution of the histograms is 256×256 over the entire 2D box (of size $5.24 \cdot 10^{-4}\mathrm{m} \times 5.24 \cdot 10^{-4}\mathrm{m}$) as before. We have also looked into the relative distance between the vortices and the antivortex with respect to time. The resulting plots when the vortex is flipped at $0.08\xi, 0.1\xi$ and 0.12ξ from its ground-state position are presented in figure 6.11. An overall oscillation of the sum of the relative distances is observed in all three cases. Compared to the case with a total vortex number of 2 in figure 5.5 and a total vortex number of 3 in figure 6.9, the

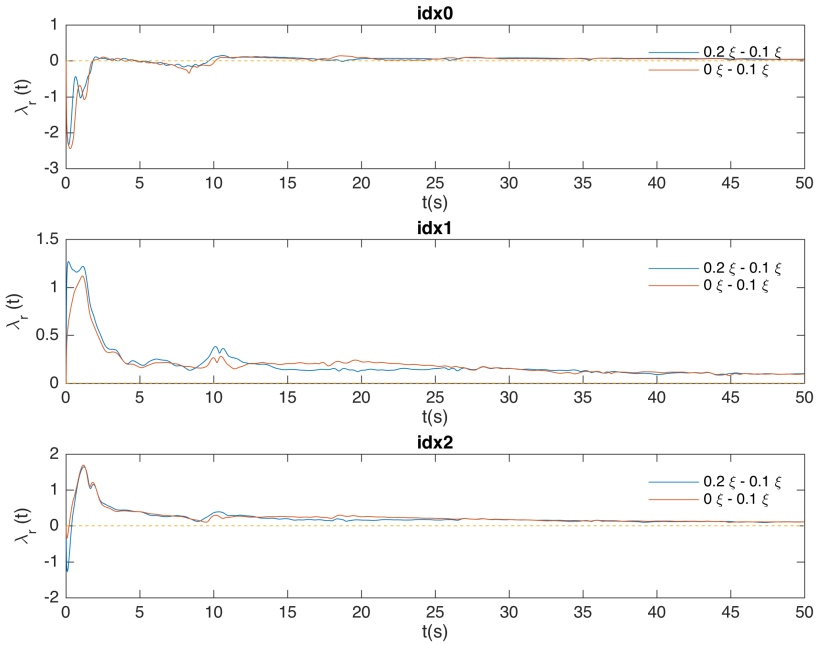

Figure 6.7: The Lyapunov exponent spectrum for individual vortices in a system of two vortices and one antivortex calculated from two sets of data with vortex flipping at 0ξ and 0.2ξ with trajectories induced by vortex flipping at 0.1ξ used as the reference trajectory. Vortex 'idx 0' denotes the flipped vortex (antivortex) and 'idx 1' and 'idx 2' are the two unperturbed vortices.

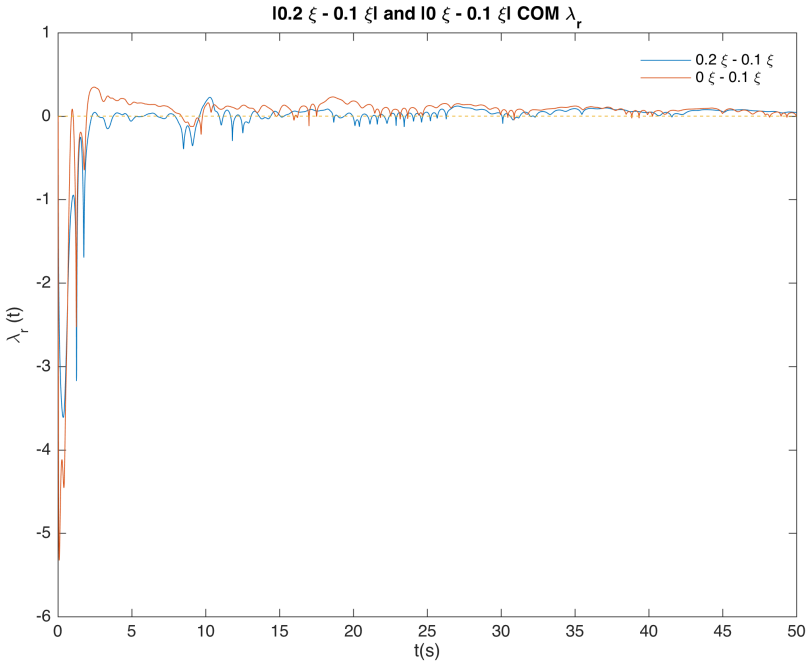

Figure 6.8: The Lyapunov exponent spectrum of the COM trajectories of the system of two vortices and one antivortex in the co-rotating frame, calculated from two sets of data where a vortex is flipped at 0ξ and 0.2ξ respectively, with trajectories induced by vortex flipping at 0.1ξ used as the reference trajectory.

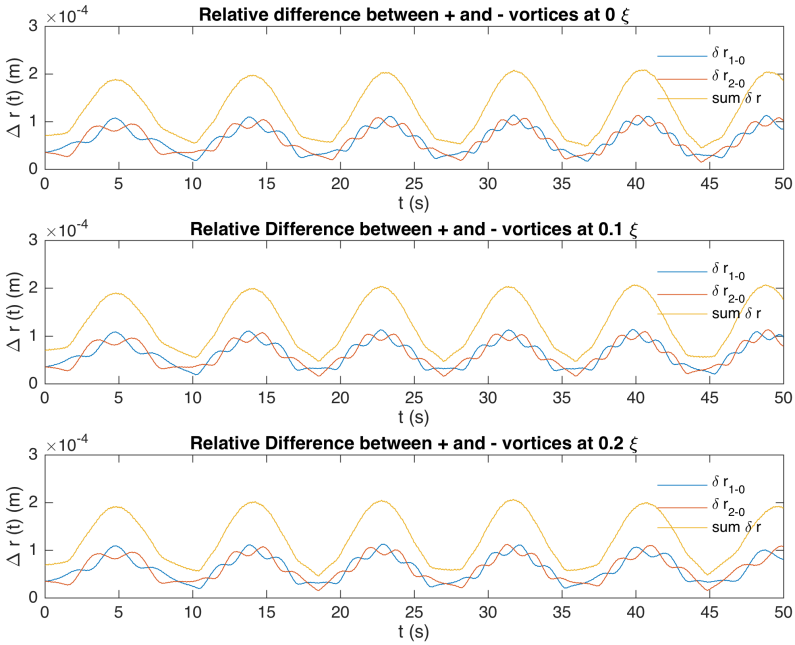

Figure 6.9: The relative distance between the antivortex and the other two vortices, denoted as δr_{1-0} and δr_{2-0} respectively, when flipping takes place right on the vortex core. The sum $\delta r = \delta r_{1-0} + \delta r_{2-0}$ is the sum of the two relative distances. The upper plot is calculated with vortex trajectories induced by vortex flipping with 0ξ offset. The middle plot is calculated with vortex trajectories induced by vortex flipping with 0.1ξ offset. The lower plot is calculated with vortex trajectories induced by vortex flipping with 0.2ξ offset from the original vortex position.

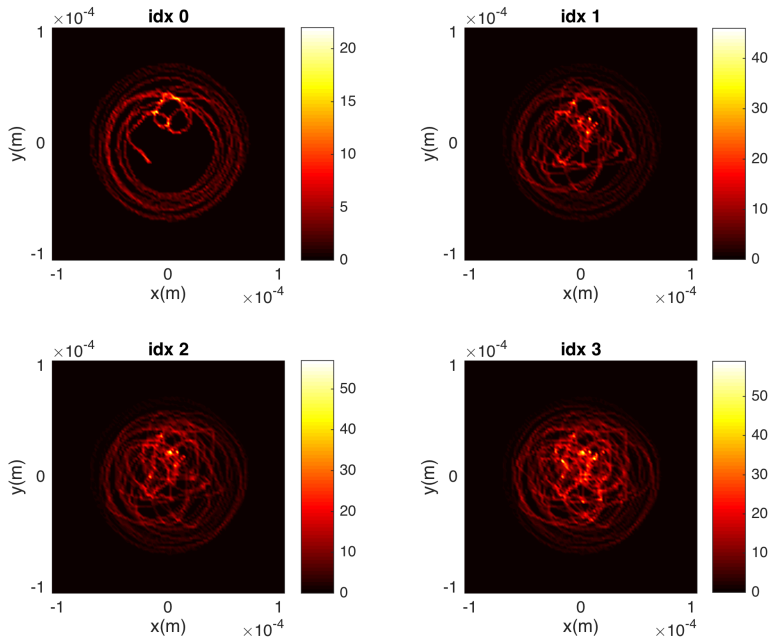

Figure 6.10: The histogram of trajectories of individual vortices in the co-rotating frame over a total time evolution of 50s, with one antivortex (idx 0) and three vortices (idx 1, idx 2, idx 3) in the BEC.

oscillations are more irregular. This irregularity is a sign of more complicated dynamics occurring in the system.

In addition to the slow oscillation, the relative distance between the antivortex and any of the other three vortices ($\delta r_{i-0},\ i = 1, 2, 3$) presents a fast oscillation. In particular, δr_{1-0} and δr_{2-0} present a more entangled oscillation in comparison to δr_{3-0}. The equal initial distance between the antivortex and these two vortices (idx 1 and idx 2) should play a role here, since this resembles figure 6.9, which shows the system of a three vortices (two vortices and one antivortex) that are initially equally distant from each other.

Figure 6.12 shows the difference between vortex trajectories from two sets of data which deviate only by a slight change in the initial position of the flipped vortex. The drastic divergence of the deviations in trajectories is another strong sign of chaotic dynamics. In addition to the observation of the divergence of the difference in trajectories, it seems that the timing of this divergence depends on the difference in the initial conditions as well. Figure 6.13 shows the difference between trajectories with a larger difference in the initial conditions. In this case a small divergence occurs much earlier around 5s after flipping. Let us now look again at the relative distance between the antivortex and the other three vortices, as well as the sum of the relative distances, in figure 6.11. The sum of the relative distances reaches its first minimum at around $t = 10$s, regardless of the flipping distance. At this minimum, these four vortices (including the antivortex) are closest to each other and the scattering between them is also stronger. This is most likely the trigger

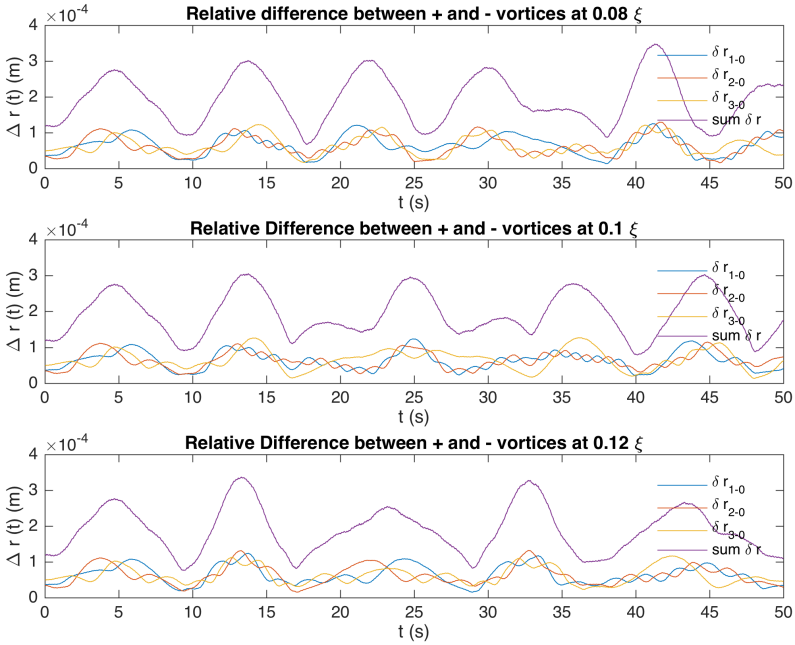

Figure 6.11: Plots show the relative distance between vortices and the antivortex, denoted as $\delta_{i-0},\ i = 1, 2, 3$. The sum of all δ_{i-0}, sumδr is also shown. The three plots show the scenario when the flipping is at 0.08ξ (upper plot), 0.1ξ (middle plot) and 0.12ξ (lower plot) away from the vortex core, respectively.

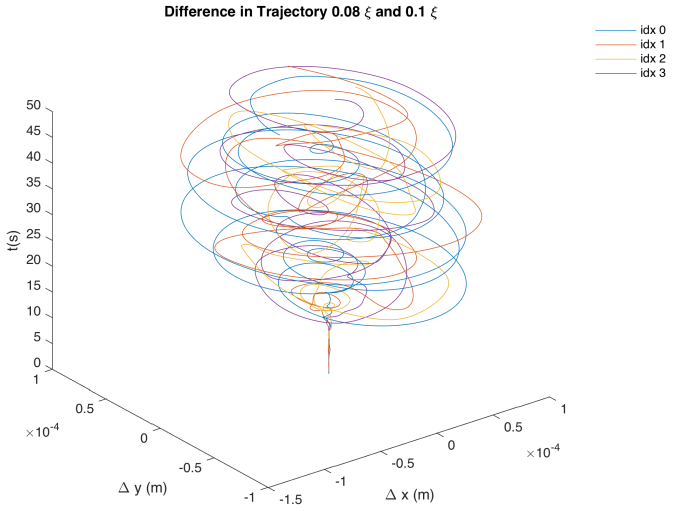

Figure 6.12: The time evolution of the difference between two trajectories of each vortex, where vortex 0 has been flipped initially 0.08ξ and 0.1ξ away from the vortex core, respectively.

for the drastic divergence of the separation between the close-by trajectories, as shown in figure 6.12.

The COC and COM trajectories of the system composed of three vortices and one antivortex in the co-rotating frame with a vortex flipped at 0.08ξ and 0.1ξ are shown in figure 6.14. The mixing of these orbits is also observed here.

All the results that we have presented so far, have shown similar, if not stronger signs of chaos than in the previous section where three vortices in a BEC were considered. We will now calculate the corresponding Lypunov exponent and SALI in the next section.

6.2.1 The Lyapunov exponent spectrum

The exact definition of the Lyapunov exponent can be found in chapter 4. We use the flipping distance from the vortex core as a parameter to manipulate the initial conditions. We choose three sets of simulations where one vortex has been initially flipped at $0.12\xi, 0.1\xi$ and 0.08ξ away from the original vortex core position. The vortex trajectories corresponding to a vortex flipped at 0.1ξ from the original vortex position is used as the reference orbit. The corresponding Lyapunov exponent spectrum is shown in figure 6.15. According to the definition of the Lyapunov exponent (which is referred to as λ_r from now on), provided a minimal difference in the initial conditions in phase space, if $\lambda_r > 0$ when $t \to \infty$, the orbit is chaotic. This has been confirmed by figure 6.15, which shows the Lyapunov exponentum spectrum of the individual vortices for the three sets of trajecto-

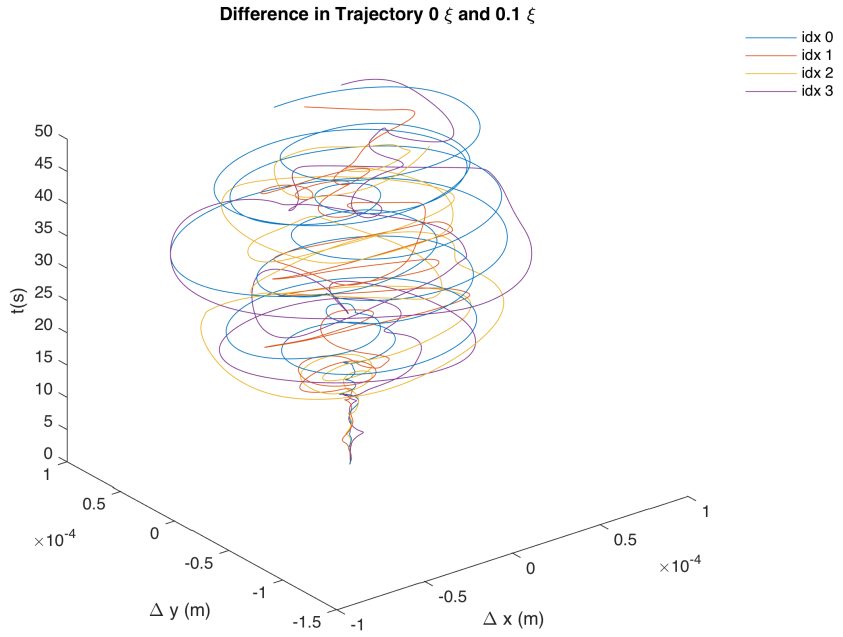

Figure 6.13: The time evolution of the difference between trajectories of each vortex, where vortex 0 has been flipped initially at 0ξ and 0.1ξ away from the vortex core, respectively.

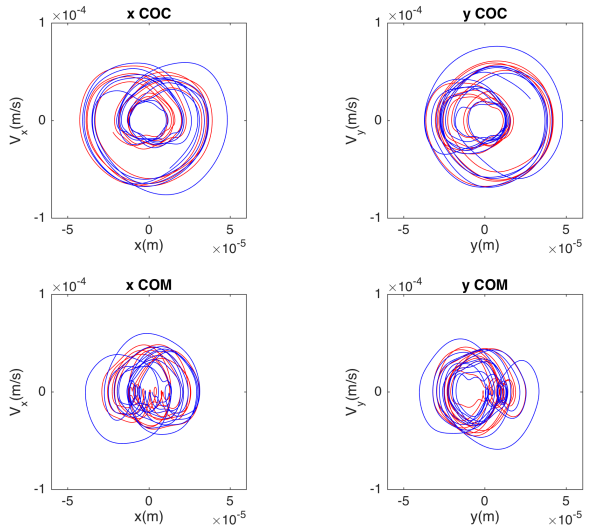

Figure 6.14: The COC and COM orbits of a system consisting of three vortices and one antivortex in phase space, (x, V_x) and (y, V_y) respectively, during 50s in the co-rotating frame. The red line indicates the trajectory of the system where the flipping of a vortex takes place at 0.1ξ from the origional vortex position, and the blue line is depicting the system's trajectory with flipping at 0.08ξ.

ries (with the flipping distances described earlier). The Lyapunov exponents, λ_r, start to stabilize at around 10s. Recall that this is also when the drastic divergence of separation between close-by trajectories occurs. λ_r remains strictly positive for all four vortices and converges slowly towards a positive value $\simeq 0.1$. We evolve the vortex dynamics for 50s, which is comparable to the current experimental life-time of BECs (Ramanathan et al. (2011)).

Instead of looking at the chaotic behaviour of individual vortices, we now study the behaviour of the entire system of vortices by exploiting the COM and COC trajectories (defined in equation (6.1)). The corresponding Lyapunov exponent spectrums are shown in figure 6.16 and 6.17. Compared to the spectrum of individual vortices, the λ_r in these two spectrums oscillates more and stays positive during this time period.

We also want to investigate how the size of the condensate, and hence the initial vortex spacing, effects the strength of the chaos. We alter the the size of the condensate in our simulation by varying the trapping frequencies in $xy-$dimensions and the total number of atoms. We have successfully constructed BECs with three different radii while ensuring the same vortex core size. The average Lyapunov exponents of COC and COM trajectories of three vortices and one antivortex (where the vortex flipping takes place right on the vortex core) inside BECs with three slightly different radii are shown in table 6.1. Lyapunov exponents are generally greater in the condensate with the smallest radius, which corresponds to smaller initial intervortex spacing. This larger Lyapunov exponent indicates a

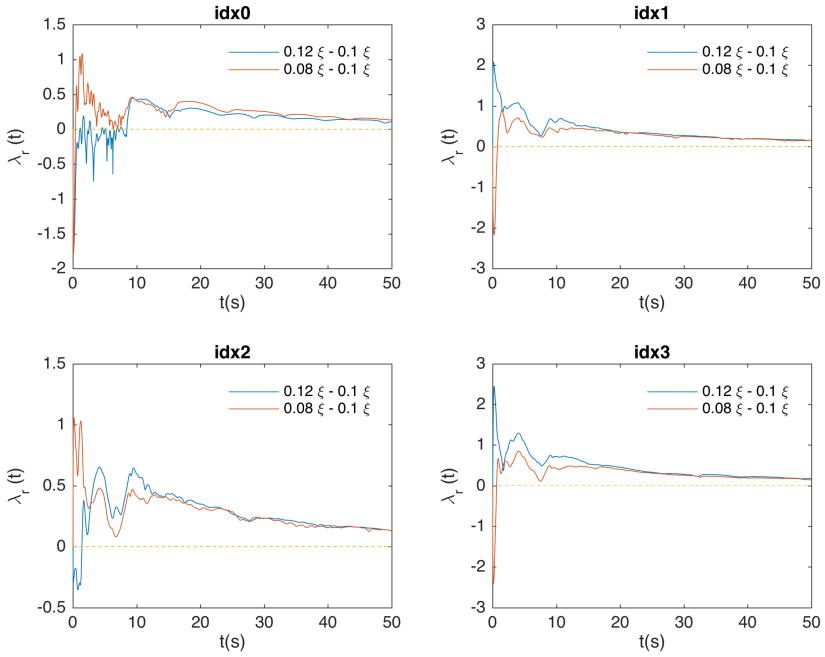

Figure 6.15: The Lyapunov exponent spectrum for each individual vortex in a BEC with three vortices and one antivortex during 50s. idx 0 is the antivortex and other three are the nonflipped vortices in the BEC. The blue lines indicate the calculated Lyapunov exponent between two trajectories induced by vortex flipping at 0.12ξ and 0.1ξ. Similarly the red lines are the Lyapunov exponents based on trajectories followed by vortex flipping at 0.08ξ and 0.1ξ.

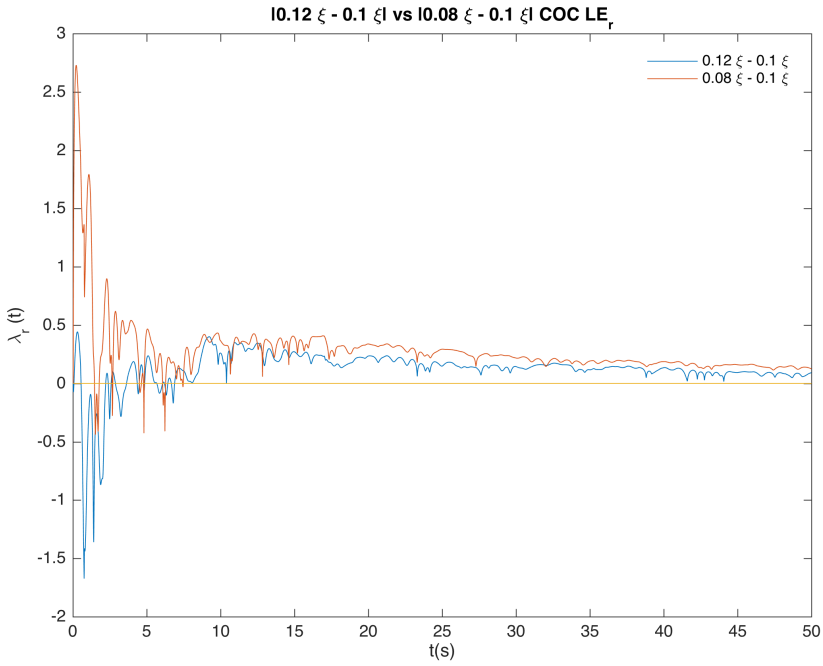

Figure 6.16: The Lyapunov exponent spectrum of COC trajectories for a system of three vortices and one antivortex in the co-rotating frame. The trajectory from vortex flipping at 0.1ξ is used as the reference orbit and trajectories from vortex flipping at 0.08ξ (blue) and 0.12ξ (red) away from the original vortex position are the close-by orbits used in calculating the corresponding Lyapunov exponent.

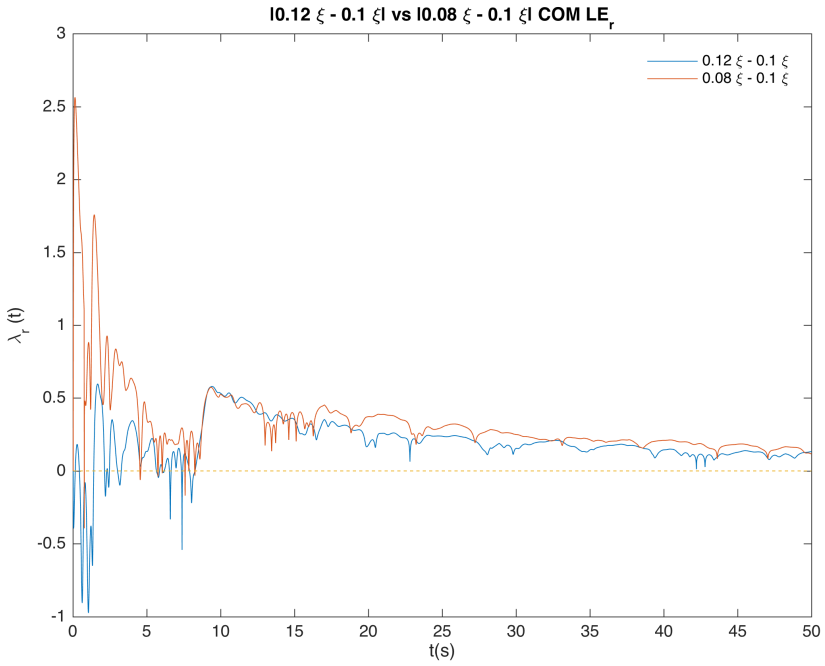

Figure 6.17: The Lyapunov exponent spectrum of COM trajectories for a system of three vortices and one antivortex in the co-rotating frame. The trajectory from vortex flipping at 0.1ξ is used as the reference orbit and trajectories from vortex flipping at 0.08ξ (blue) and 0.12ξ (red) away from the original vortex position are the close-by orbits used in calculating the corresponding Lyapunov exponent.

stronger chaos which is induced by stronger initial intervortex scatterings.

Table 6.1: A comparison between the averaged Lyapunov exponent calculated over the time period between $[45\text{s}, 50\text{s}]$ of the COM and COC trajectories of three vortices and one antivortex. The trajectories originate from vortex flipping at respectively 0.12ξ and 0ξ away from the original vortex core position, with 0.1ξ used as the reference orbits, inside BECs with three different condensate radii R.

λ / R	0.12ξ vs 0.1ξ		0ξ vs 0.1ξ	
	COC	COM	COC	COM
$1.01 \cdot 10^{-4}\text{m}$	0.08	0.08	0.07	0.11
$1.07 \cdot 10^{-4}\text{m}$	0.06	0.08	0.05	0.07
$2.68 \cdot 10^{-4}\text{m}$	0.03	0.05	0.05	0.07

6.2.2 The smaller alignment index (SALI)

In addition to calculating the Lyapunov exponent spectrum, we have also applied SALI to our data. SALI is a good indicator for testing the random alignment between the deviation vector of two close-by orbits. According to Skokos et al. (2004), for chaotic orbits, SALI decreases exponentially to zero. However this decay of the SALI value hasn't been observed in our results. For the course of time that we looked into, the reason for the absence of the decay maybe due to a sticky feature which has also been described in Antonopoulos et al. (2010) with relevance with weak chaos. What we mean by this sticky feature, is a delay of the decay when the chaos is weak. Due to the limitation of the computing time, it is not practical to increase the evolution time of the condensate by much. Alternative ways of comparing SALI are hence needed.

Instead of looking at the absolute value of SALI, we have decided to compare the SALI spectrum of four vortices with one of them flipped, with the SALI spectrum of four vortices when one of them re-imprinted, but not flipped. The re-imprinted case is described in chapter 5 where a vortex is annihilated and re-imprinted to induce motions of vortices in the co-rotating frame. We also regulate where to re-imprint the vortex in a same way as we do when flipping from a vortex to an antivortex. For the calculation of SALI, we have used three sets of trajectories, with vortex flipping or re-imprinting at 0.2ξ, 0.1ξ and 0ξ away from the original vortex core in a system of four vortices. For more details, see section 5.3. The SALI spectrum of the COC trajectories of three vortices and one antivortex is shown in figure 6.18. In this spectrum the SALI value oscillates rapidly in the range $10^0 - 10^{-4}$. This is a sign of the random alignment of deviation vectors between two nearby orbits. The SALI spectrum of four equally charged vortices when one of them re-imprinted slightly off-set from its original position is shown in figure 6.19. The SALI value stays constant at around 10^{-1}. The lower plot in figure 6.19 shows the value of the two quantities of which SALI is based on (see section 4.2 for the definition of SALI). From this plot, we can tell that the two deviation vectors are constantly aligned in the opposite direction. The opposite alignment is possibly due to the fact that the two near-by orbits (re-imprinting at

0.2ξ and 0ξ) are symmetric about the reference orbit (re-imprinting at 0.1ξ) in the position space. A comparison between figure 6.18 and figure 6.19 gives a good contrast between the regular behaviour (see discussion in section 5.3) and the chaotic behaviour.

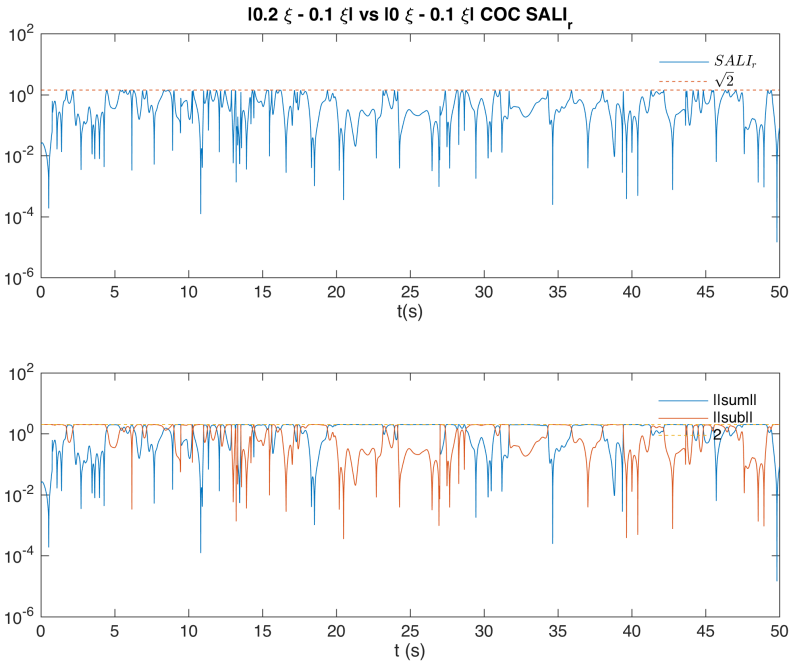

Figure 6.18: The upper plot: the SALI spectrum for the system with three vortices and one antivortex with vortex flipping at 0ξ, 0.1ξ and 0.2ξ from its original position, applied as near-by orbits. The lower plot: the comparison between the two components of SALI, $\|\text{sum}\|$ and $\|\text{sub}\|$, which are respectively the sum and difference of the two deviation vectors (flipping at 0ξ w.r.t. 0.1ξ and flipping 0.2ξ w.r.t. 0.1ξ). The smaller of the two components gives the value of SALI.

For systems consisting of more than two vortices, by perturbing the initial conditions and tuning the perturbation slightly, the vortex trajectories can be changed drastically. We have also investigated the vortex dynamics of a BEC with five and six vortices with one of them flipped. In both scenarios, the vortex dynamics is classified to be chaotic with the same procedures as described in this chapter. We assume we keep the atomic cloud at 0K and it is dissipation free. The applied perturbation in our system is vortex flipping, namely reversing the direction of circulation of one of the vortices in the system which is the generated ground state by employing imaginary time propagation as described in Chapter 3.

The free parameter of this perturbation is where the flipping takes place relative to the original vortex core position. We have performed an analysis on vortex configurations composed of up to 6 vortices. Systems containing 3 or more vortices have shown signs

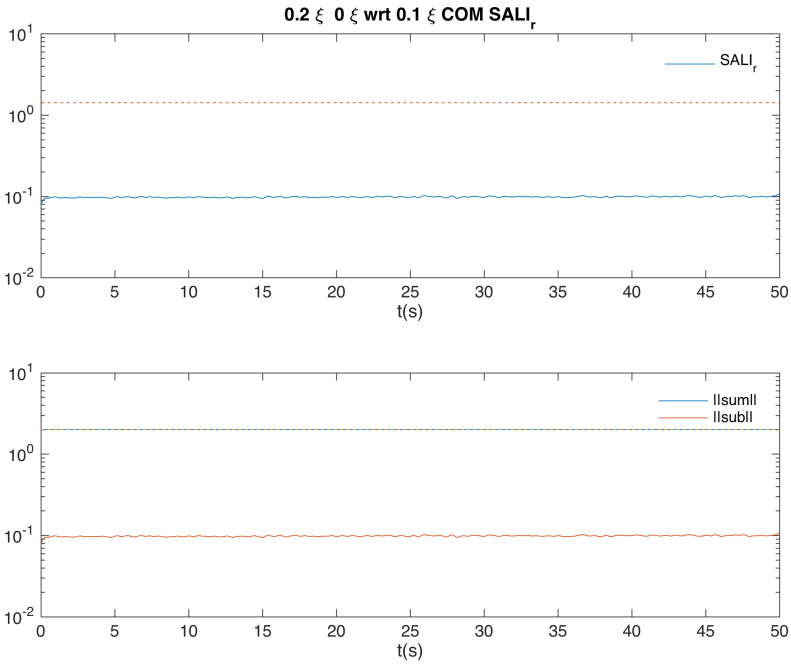

Figure 6.19: The upper plot: the SALI spectrum for a system with four vortices where one of the vortices is shifted slightly off-set from its original position at respectively 0ξ, 0.1ξ and 0.2ξ. The lower plot: the comparison between two components, $\|\text{sum}\|$ and $\|\text{sub}\|$, which are respectively the sum and difference of the two deviation vectors (flipping at 0ξ w.r.t. 0.1ξ and flipping 0.2ξ w.r.t. 0.1ξ). The smaller one of the two components is defined as the value of SALI.

of chaotic behaviour. We have further confirmed this chaotic behaviour by computing the Lyapunov exponent spectrum, and also computing the smaller alignment index (SALI).

Chapter 7

Alternative approaches

All the previous analyses that have been performed in this work are based on the order parameter (wavefunction) in position space, $\Psi(\boldsymbol{r})$. They have enabled us to identify, flip and track the location of vortices excellently. At the same time, we also want to investigate other representations of the BEC, such as the order parameter in phase space and the the Wigner function, which gives the quasi-probability distribution. We discuss these two representations and their application to vortex dynamics in this chapter.

7.1 Momentum distribution

Our description of BECs so far has concentrated on the wavefunction in position space, $\Psi(x, y)$. Since we are exclusively interested in the motion of quantum vortices in a BEC, which are dictated by their velocity field, we also investigate the wavefunction of the condensate in momentum space, $\Psi(p_x, p_y)$, obtained by Fourier transforming $\Psi(x, y)$. The momentum distribution of the BEC, $\Psi(p_x, p_y)$ can be measured by taking the time-of-flight image of a BEC, after turning off the harmonic trap (Abo-Shaeer et al. (2001)Seo et al. (2014)).

We now compute the momentum distribution of a BEC with a few vortices. By taking the Fourier transform of the ground state wavefunction of a BEC with 3 singly charged vortices (with positive phase winding), we show in figure 7.1, the density distribution in momentum space as well as the corresponding momentum space phase of the wavefunction, and the real and imaginary components of the wavefunction in momentum space. A comparison between the momentum distribution and the wavefunction phase indicate that the locations of the quantum vortices are at the dip in the momentum distribution (dark blue regions close to the centre in figure 7.1 c)) and at the singular points in the phase plot (see figure 7.1 d)).

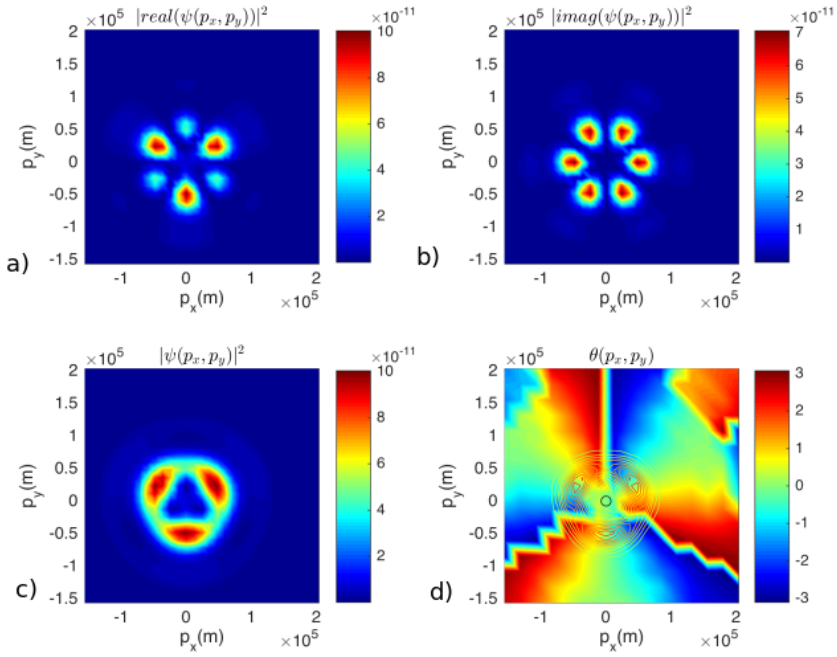

Figure 7.1: The wavefunction of the BEC in momentum space,$\Psi(p_x, p_y)$, with 3 singly charged vortices with positive phase winding. Subplot a) shows the real component of $\Psi(p_x, p_y)$, b) shows the imaginary component of $\Psi(p_x, p_y)$, c) is the momentum distribution $|\Psi(p_x, p_y)|^2$ and d) shows the corresponding phase $\theta(p_x, p_y) = \arctan(\Im(\Psi(p_x, p_y))/\Re(\Psi(p_x, p_y)))$ overlayed by a contour plot of $|\Psi(p_x, p_y)|^2$.

For the aim of this work, the wavefunction of a BEC with three vortices where one of them is flipped (giving two vortices and one antivortex) in momentum space is of greater interest. The corresponding density and phase in momentum space of the condensate wavefunction 0.01s after flipping one of the three vortices is shown in figure 7.2.

A comparison between figure 7.1 of a BEC with three vortices and figure 7.2 of a BEC with two vortices and one antivortex shows that vortices with opposite charges appear to annihilate each other, while vortices with equal charges remain visible in the momentum distribution. This annihilation is most likely due to the fact that for a vortex and an antivortex (opposite circulation) that reside at the same position, their corresponding distributions in momentum space are the opposite of each other. Another observation is that the phase plot of a BEC with one flipped vortex becomes very noisy. This makes developing a good algorithm for vortex tracking in momentum space more challenging.

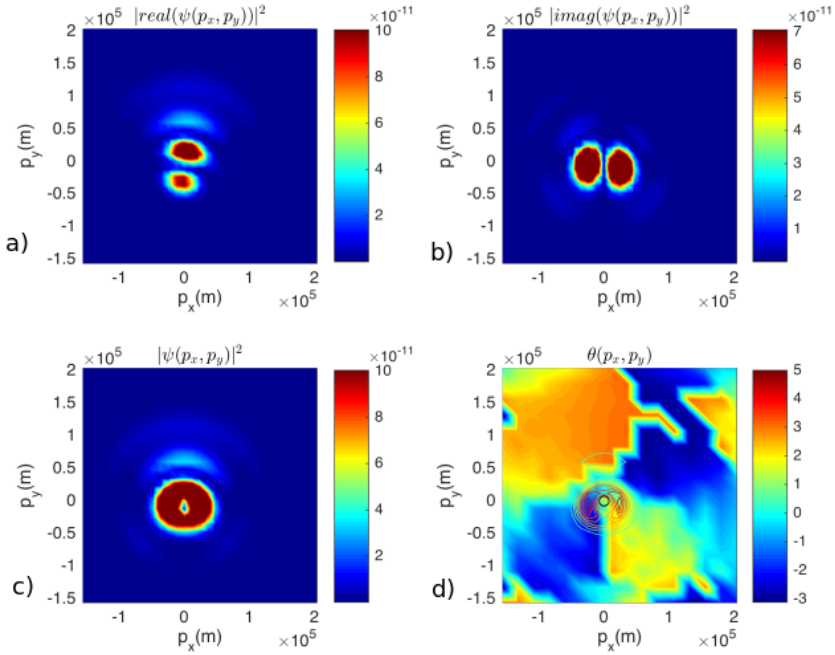

Figure 7.2: The wavefunction of a BEC in momentum space,$\Psi(p_x, p_y)$, with 3 singly charged vortices, 2 with positive phase winding and 1 with negative phase winding, 0.01s after vortex flipping. Supolot a) shows the real component of $\Psi(p_x, p_y)$, plot b) shows the imaginary component of $\Psi(p_x, p_y)$, c) is the density distribution in momentum space $|\Psi(p_x, p_y)|^2$ and d) is the corresponding phase $\theta(p_x, p_y) = \arctan(\Im(\Psi(p_x, p_y))/\Re(\Psi(p_x, p_y)))$ together with a contour plot of the $|\Psi(p_x, p_y)|^2$.

For the purpose of completeness, the momentum distribution of a BEC with 4 singly charged vortices (with positive phase winding) is shown in figure 7.3 and the distribution in

momentum space of a BEC with three vortices (positive phase winding) and one antivortex (negative phase winding), 0.01s after vortex flipping, is shown in figure 7.4.

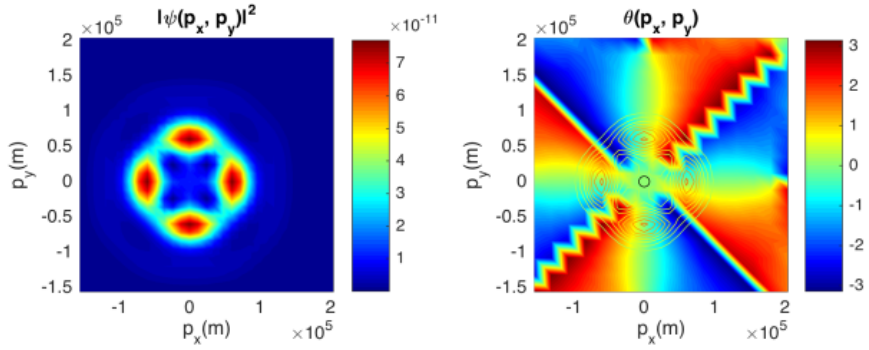

Figure 7.3: The wavefunction of a BEC in momentum space,$\Psi(p_x, p_y)$, with 4 singly charged vortices with positive phase winding. The left figure shows the density distribution in momentum space, $|\Psi(p_x, p_y)|^2$. The right figure gives the corresponding phase $\theta(p_x, p_y) = \arctan(\Im(\Psi(p_x, p_y))/\Re(\Psi(p_x, p_y)))$ superimposed by a contour plot of $|\Psi(p_x, p_y)|^2$.

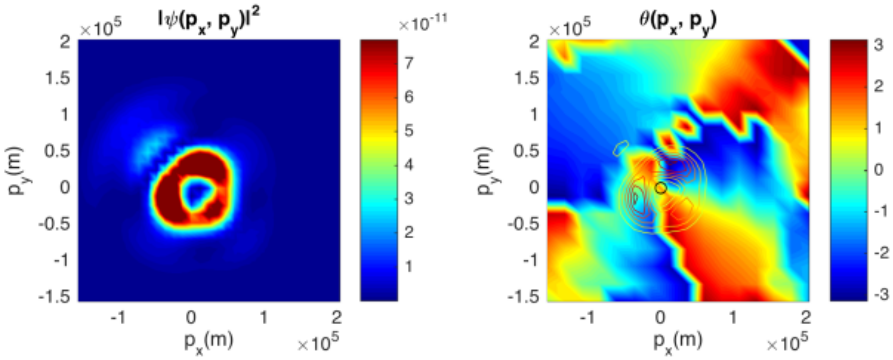

Figure 7.4: The wavefunction of a BEC in momentum space,$\Psi(p_x, p_y)$, with 3 singly charged vortices, 2 with positive phase winding and 1 with negative phase winding 0.01s after vortex flipping. The left figure is the density distribution in momentum space $|\Psi(p_x, p_y)|^2$. The right figure is the phase plot, aka. $\theta = \arctan(\Im(\Psi)/\Re(\Psi))$ together with a contour plot of $|\Psi|^2$.

By looking at the momentum distribution, we were hoping to gain information about the momentum of vortices, as all of the previously discussed quantities in phase space are built only on the vortex position and corresponding velocity, (calculated by taking the time derivative of the vortex position). However, we found that the phase of the complex wavefunction in momentum space after flipping one of vortices presented some irregularity and noise during the time evolution. This makes tracking the vortex positions in momentum space very challenging. In addition, due to the opposite circulation of the antivortex,

its momentum distribution overlaps with the momentum distribution of a vortex located symmetrically about the origin $(x, y) = (0, 0)$ of the antivortex. One way of obtaining a momentum space with better resolution is to expand the 2D computational box we use to model the BEC, or decrease the spatial resolution of the BEC in position space. Both solutions are worth investigating further. In the next section, we will be looking at a function that describes quantum states in full phase space, the Wigner function or quasi-probability distribution.

7.2 Wigner function

The Wigner function was first introduced by Eugene Wigner back in 1932 (Wigner (1932)). It is generally recognised as the mapping of a density matrix in position space into a probability distribution in phase space. The Wigner function is often referred to as a quasi-probability distribution, due to the fact that it can take negative values.

The definition of the Wigner function is the following,

$$W(x, y, p_x, p_y) := \frac{1}{\pi\hbar} \int_{-\infty}^{\infty} \Psi^*(x+\nu, y+\mu)\Psi(x-\nu, y-\mu)e^{2i(p_x\nu+p_y\mu)/\hbar}d\nu d\mu. \quad (7.1)$$

The Wigner function is real and normalised over all phase space as $\int\int W(\mathbf{r}, \mathbf{p})\mathrm{d}\mathbf{r}\mathrm{d}\mathbf{p} = 1$. The difficulty in calculating the Wigner function numerically, comes from the fact that for a 2-dimensional BEC, the Wigner function is a 4-dimensional array. Our simulation resolves the spatial extent with a grid of 1024×1024 points. This leads to a numerically calculated Wigner function of our system of the size 1024^4, which exceeds the memory resources we have available.

To overcome this, instead of calculating the Wigner function for the entire system, we have calculated the Wigner function around the vortices, or more specifically a grid of 11×11 points symmerically around each vortex. The calculated Wigner function around the antivortex of a BEC consisting of one antivortex (labelled 'idx 0') and three vortices 0.02s after vortex flipping, is shown in figure 7.5. The Wigner functions around the other three vortices (labelled 'idx 1', 'idx 2', and 'idx 3') are given in the appendix (see appendix 1, figures 1, 2 and 3). In these figures, the Wigner functions are illustrated by fixing two of the four parameters (x, y, p_x, p_y) each time, to their corresponding values at the vortex core. In other words, x and y are fixed to the location of the antivortex in the condensate and p_x and p_y are fixed to the corresponding momentum. A similar method was used in Banerji et al. (2016), where the Wigner function of a 2D single on-centre optical vortex is calculated. In this article, the Wigner function is also illustrated by fixing two parameters per time instant (which gives in total six possible combinations). Among the six plots of the Wigner functions, $W(x, p_x)$ and $W(y, p_y)$ present the same structure, while $W(x, p_y)$ and $W(y, p_x)$ have the same structure. Hence in our figures, we are only showing $W(x, y)$, $W(x, p_x)$, $W(y, p_x)$ and $W(p_x, p_y)$.

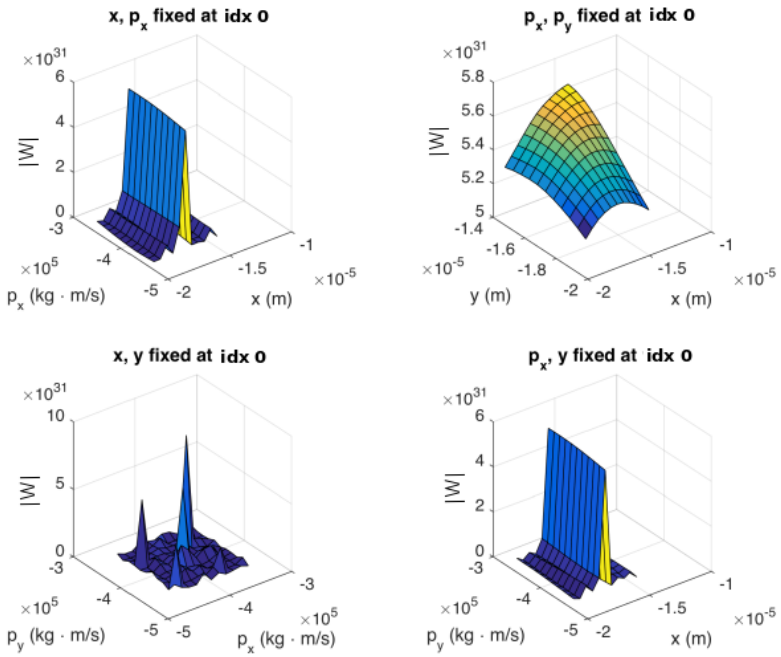

Figure 7.5: The calculated Wigner function, $W(x, y, p_x, p_y)$ around the antivortex labelled by index 0, 'idx 0', in our simulated BEC, consisting of three vortices and one antivortex. The four plots of the absolute Wigner function $|W|$ are obtained by fixing y and p_y (upper left plot), x and y (upper right plot), p_x and p_y (lower left plot) and x and p_y (lower right plot) at vortex core.

In order to understand what the Wigner function of a single vortex in a BEC looks like, we have artificially constructed a central vortex in a 2D BEC with the same radius and a resolution of 30×30 grid points over a 2D box of the same size as our numerical simulations. The exact expression that we have used for the condensate wavefunction is

$$\psi(x,y) = \begin{cases} \tilde{n}\sqrt{1 - \frac{x^2+y^2}{R^2} \cdot \left(1 - \frac{1}{1+\frac{x^2+y^2}{\xi^2}}\right)} \cdot \exp\left(i \arctan(\frac{y}{x})\right), & \text{if } x^2+y^2 < R^2, \\ 0, & \text{if } x^2+y^2 \geq R^2, \end{cases}$$

here $R = 1.71579 \times 10^{-4}$m is the radius of the condensate, which is equal to the condensate radius from our simulation, and $\xi = 5.11 \times 10^{-6}$m is equal to the numerical healing length of the simulated BEC. $\tilde{n}$ is a renormalisation constant, $\tilde{n} = (\int dxdy\psi)^{-1}$. The corresponding density and phase plot of this constructed condensate is shown in figure 7.6. Using this constructed condensate wavefunction, the Wigner function over the entire condensate has been calculated, and is shown in figure 7.7. Here $x,\ y,\ p_x$, and p_y are taken to be zero when being fixed. $W(x,y) = W(x,y,p_x = 0, p_y = 0)$, shown in (a) in figure 7.7, has a dip at the centre ($(x,y) = (0,0)$); $W(x,p_x) = W(x, y = 0, p_x, p_y = 0)$ in (b) and $W(x,p_y) = W(x, y = 0, p_x = 0, p_y)$ in (c) have the same structure; and $W(p_x,p_y) = W(x = 0, y = 0, p_x, p_y)$ in (d) is equal to zero over the entire condensate. It seems that when $x = 0, y = 0$, the Wigner function is zero, which we can see from all the four plots in figure 7.7. This is a good indication of the zero density at the centre of the condensate, indicating the existence of the vortex. However this dip is not observed in the corresponding $W(x,y)$ around the antivortex from our numerical simulation in figure 7.5. In the future, when we can sample over a greater region around vortices, this dip might be observed. The plot of $W(p_x,p_y)$ (with x, p_x fixed) in figure 7.5 is mostly zero except a few peaks scattered around in the calculated region. We are not able to conclude at this stage whether this is physical and indicates the vortex momentum, or a numerical error. More investigations need to be done to understand this in future work.

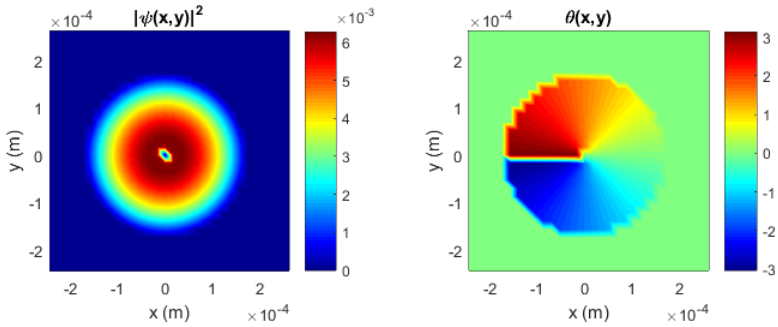

Figure 7.6: The density (left) and phase plot (right) of the constructed condensate, containing one central vortex with counterclockwise circulation.

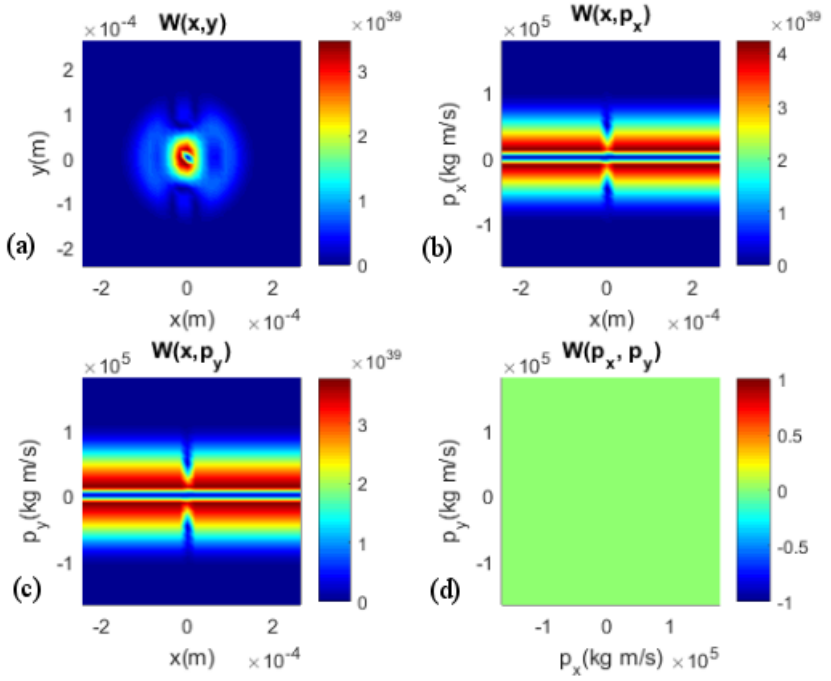

Figure 7.7: The Wigner function of a constructed condensate containing a central vortex with counterclockwise circulation. (a) plots the Wigner function, $W(x, y, p_x = 0, p_y = 0)$; (b) plots Wigner function, $W(x, y = 0, p_x, p_y = 0)$; (c) plots Wigner function, $W(x, y = 0, p_x = 0, p_y)$; (b) plots Wigner function, $W(x = 0, y = 0, p_x, p_y)$.

Chapter 8

Conclusions

The aim of this work has been to study quantum chaos in a BEC which consists of a few vortices. In this thesis, we have demonstrated that chaotic dynamics can be induced for few vortex systems, by starting from a vortex lattice and reversing the direction of circulation of a single vortex. The chaotic dynamics were confirmed by two chaos indicators.

All our analyses are based on a numerically simulated 2D rotating BEC, trapped inside a harmonic potential. The main simulation is implemented using GPU computing (O'Riordan and Busch (2016)), which has proven to have excellent performance in embarrassingly parallel problems. The phase imprinting technique has been applied to create, annihilate and flip vortices. This method is highly experimentally relevant (Dobrek et al. (1999), Möttönen et al. (2003), Brachmann et al. (2011)).

During this work, by using the phase imprinting technique, we have applied two types of perturbations to the generated ground state of a BEC with a few vortices. One perturbation applied is to annihilate one of the pre-existing vortices in the system and create a new vortex (with the same circulation) a small distance away from the original vortex site. This perturbation induces the vortices to rotate relative to the co-rotating frame, while preserving the vortex lattice structure. The direction of rotation depends on the exact location the vortex is re-imprinted. The other type of perturbation applied is vortex flipping, namely annihilating the original vortex and creating an antivortex (with opposite circulation) within the healing length of the original vortex site. We have applied vortex flipping on rotating ground state configurations of condensates with up to six vortices. It has been confirmed, with the help of two chaos indicators, that for systems with a vortex number greater than three, chaotic dynamics are successfully created by vortex flipping. The two chaos indicators applied are the Lyapunov exponent and the smaller alignment index (SALI). In particular, the Lyapunov exponent gives a clear sign of chaotic behaviour, as it is found to be positive.

In addition to tracking individual vortex dynamics and computing the Lyapunov ex-

ponent and SALI, alternative approaches have also been applied to gain more information about the vortex dynamics. In an attempt to determine the momentum of quantum vortices, we calculated the momentum distribution of the BEC. However, due to the low resolution in momentum space, it is difficult to follow vortex trajectories in momentum space. A comprise between the resolution of the wavefunction in position space and the resolution in momentum space has to be made. How this should be performed needs to be resolved in the future. Additionally, the Wigner function, which gives a description of the quantum states in phase space has been calculated. However, due to the complexity of the numerical calculation, further investigation is needed in order to fully utilise the properties of the Wigner function for this system.

One of the initial motivations behind this work is to gain a more solid understanding of quantum chaos and eventually draw a connection between quantum chaos and quantum turbulence. The next step with this project is to potentially study a greater number of vortices and apply vortex flipping on more than one vortex. With this procedure, the dynamics may transit into quantum turbulence.

Bibliography

A. T. Conlisk, Y. G. G., Elliott, G. S., 1989. Chaotic motion of an array of vortices above a flat wall. Physics of Fluids A: Fluid Dynamics 1, 704–717.

Abo-Shaeer, J. R., Raman, C., J. M. Vogels, W. K., 2001. Observation of vortex lattices in Bose–Einstein condensates. Science 292 (5516), 476–479.

Allen, J. F., 1938. Flow of liquid Helium II. Nature 141 (75).

Anderson, M. H., Ensher, J. R., Matthews, M., C. E. Wieman, E. A. C., 1995. Observation of Bose–Einstein condensation in a dilute atomic vapor. Science, New Series 269 (5221), 198–201.

Antonopoulos, C., Basios, V., Bountis, T., 2010. Weak chaos and the "melting transition" in a confined microplasma system. Physical Review E 81 (1), 016211.

Aref, H., 1983. Integrable, chaotic, and turbulent vortex motion in two-dimensional flows. Annual Reviews of fluid mechanics 15, 345–89.

Banerji, A., Singh, R. P., Banerjee, D., Bandyopadhyay, A., 2016. Generating a perfect quantum optical vortex. Physical Review A 94 (053838).

Bauke, H., Keitel, C. H., 2011. Accelerating the Fourier split operator method via graphics processing units. Computer Physics Communications 182 (12), 2454–2463.

Benitez, P., Losada, J. C., Benito, R. M., Borondo, F., 2015. Using the small alignment index chaos indicator to characterize the vibrational dynamics of a molecular system: Linc-licn. Physical Review E 92, 042918.

Bloch, I., Dalibard, J., Zwerger, W., Jul 2008. Many-body physics with ultracold gases. Rev. Mod. Phys. 80, 885–964.
URL https://link.aps.org/doi/10.1103/RevModPhys.80.885

Brachmann, J. F. S., Bakr, W. S., Gillen, J., Peng, A., Greiner, M., 2011. Inducing vortices in a Bose–Einstein condensate using holographically produced light beams. Optics Express 19 (14), 12984–12991.

Butts, D. A., Rokhsar, D. S., 1999. Predicted signature of rotating Bose–Einstein condensates. Nature 397, 327–329.

Chevy, F., Madison, K. W., Dalibard, J., 2000. Measurement of the angular momentum of a rotating Bose–Einstein condensate. Physics Review Letter 85 (11), 2223–2227.

Dobrek, L., Gajda, M., Lewenstein, M., Sengstock, K., Birkl, G., Ertmer, W., Nov 1999. Optical generation of vortices in trapped Bose–Einstein condensates. Physics Reviews A 60, R3381–R3384.
URL https://link.aps.org/doi/10.1103/PhysRevA.60.R3381

Fangohr, H., Cox, S. J., de Groot, P. A. J., 2001. Vortex dynamics in two-dimensional systems at high driving forces. Physical Review B 64, 064505.

Fetter, A. L., 2009. Rotating trapped Bose–Einstein condensates. Review of Modern Physics 81 (647), 1–44.

Fläschner, N., B.S. Rem, M. T., D. Vogel, D.-S. L., Sengstock, K., 2016. Experimental reconstruction of the Berry carvature in a Floquet Bloch band. Science 352 (6289), 1091–1094.

Foster, C., 2002. vortutils: Utilities for finding vortices in complex fields. https://github.com/c42f/vortutils, [Online; accessed 2017].

Frisch, A., Mark, M., Aikawa, K., Ferlaino, F., J. L. Bohn, C. M., Petrov, A., Kotochigova, S., 2014. Quantum chaos in ultracold collisions of gas-phase Erbium atoms. Nature 507, 475–479.

Gradinaru, V., 2007. Strang splitting for the time-dependent schrödinger equation on sparse grids. Siam Journal on Numerical Analysis 39 (12), L179–L184.

Grimm, R., Weidemüller, M., Ovchinnikov, Y. B., 2000. Optical dipole traps for neutral atoms. Advances in Atomic, Molecular and Optical Physics 42, 95–107.

Haldane, F. D. M., Wu, Y.-S., 1985. Quantum dynamics and statistics of vortices in two-dimensional superfluids. Physical Review Letters 55 (26), 2887–2890.

Kapitza, P., 1938. The super-fluidity in liquid Helium II. Nature 141 (74).

Keeton, C., 2014. Principles of Astrophysics. Springer.

Kellert, S. H., 1993. In the wake of chaos: Unpredictable order in dynamical systems. University of Chicago Press.

Kyriakopoulos, N., Koukouloyannis, V., Skokos, C., Kevrekidis, P. G., 2014. Chaotic behavior of three interacting vortices in a confined Bose–Einstein condensate. Chaos 24 (024410), 1–12.

Leggett, A. J., 1999. Superfluidity. Reviews of Modern Physics Supplement (71), 318–323.

Madison, K. W., Chevy, F., Wohlleben, W., Dalibard, J., 2000. Vortex formation in a stirred Bose–Einstein condensate. Phys. Rev. Lett 84 (5), 806–809.

Möttönen, M., Mizushima, T., Isoshima, T., Salomaa, M. M., Machida, K., Aug 2003. Splitting of a doubly quantized vortex through intertwining in Bose–Einstein condensates. Physics Reviews A 68, 023611.
URL https://link.aps.org/doi/10.1103/PhysRevA.68.023611

Murty, G. S., Rao, K. S., 1970. Numerical study of the behaviour of a system of parallel line vortices. Journal of Fluid Mechanics 40 (3), 595–602.

Nobelprize.org, 1997. The Nobel Prize in Physics 1997. https://www.nobelprize.org/nobel_prizes/physics/laureates/1997/, [Web. 17 Jul 2017].

Nobelprize.org, 2001. The Nobel Prize in Physics 2001. http://www.nobelprize.org/nobel_prizes/physics/laureate/2001/, [Web. 17 Jul 2017].

Nobelprize.org, 2003. The Nobel Prize in Physics 2003. http://www.nobelprize.org/nobel_prizes/physics/laureate/2003/, [Web. 17 Jul 2017].

O'Riordan, L. J., Busch, T., Nov 2016. Topological defect dynamics of vortex lattices in Bose–Einstein condensates. Physical Review A 94, 053603.
URL https://link.aps.org/doi/10.1103/PhysRevA.94.053603

O'Riordan, L. J., Morgan, T., Crowley, N., 2017. Gpu:phasegineering release, zenodo. https://gitbub.com/mlxd/gpue.

Pethick, C. J., Smith, H., 2008. Bose–Einstein Condensation in Dilute Gases. Cambridge.

Phillips, W. D., 1998. Laser cooling and trapping of neutral atoms. Reviews of Modern Physics 70 (3), 721–741.

Pritchard, D. E., 1983. Cooling neutral atoms in a magnetic trap for precision spectroscopy. Physical Review Letters 51 (15), 1336.

Ramanathan, A., Wright, K. C., Muniz, S. R., Zelan, M., 3rd Hill, W. T., Lobb, C. J., Helmerson, K., Phillips, W. D., Campbell, G. K., 2011. Sueprflow in toroidal Bose–Einstein condensate: an atom circuit with a tunable weak link. Physical Review Letters 106 (13), 130401.

Seo, S. W., Choi, J., Shin, Y., 2014. Free expansion of quasi-2D Bose–Einstein condensates with quantized vortices. Journal of the Korean Physical Society 64 (1), 53–57.

Shankar, R., 1994. Principle of Quantum Mechanics. Plenum Press.

Skokos, C., 2001. Alignment indices: a new, simple method for determining the ordered or chaotic nature of orbits. Journal of Physics A: Mathmatical and General 34 (47), 10029–10043.

Skokos, C., Antonopoulos, C., Bountis, T. C., Vrahatis, M. N., 2002. Smaller alignment index (SALI): Determining the ordered or chaotic nature of orbits in conservative dynamical systems.

Skokos, C., Antonopoulos, C., Bountis, T. C., Vrahatis, M. N., 2004. Detecting order and chaos in Hamiltonian systems by the SALI method. Journal of Physics A: Mathematical and General 37 (24), 6269–6284.

Slater, J. C., 1951. A simplification of the Hartree-Fock method. Physical Review 81 (3), 385–390.

Speetjens, M. F. M., Meleshko, V. V., van Heijst, G. J. F., 2014. Spectral analysis of point-vortex dynamics: first application to vortex polygons in a circular domain. Fluid Dynamics Research 46 (031402).

Steane, A. M., Chowdhury, M., Foot, C. J., 1992. Radiation force in the magneto-optical trap. Journal of the Optical Society of America B 9 (12), 2142–2158.

Suchet, D., Rabinovic, M., Reimann, T., Kretschmar, N., Sievers, F., Salomon, C., Lau, J., Goulko, O., Lobo, C., Chevy, F., 2016. Analog simulation of Weyl particles with cold atoms. Europhysics Letters 114 (2), 26005.

Vallejo, J. C., Sanjuán, M. A. F., 2013. Predictability of orbits in coupled systems through finite-time Lyapunov exponents. New Journal of Physics 15, 113064.

Voglis, N., Contopoulos, G., Efthymiopoulos, C., 1999. Detection of ordered and chaotic motion using the dynamical spectra. Celestial Mechanics and Dynamical Astronomy 73 (1-4), 211–220.

Wigner, E., 1932. On the quantum correction for thermodynamic equilibrium. Physical Review 40, 749–759.

Wisniacki, D. A., Pujals, E. R., Borondo, F., 2007. Vortex dynamics and their interactions in quantum trajectories. Journal of Physics A: Mathematical and Theoretical 40, 14353–14368.

Wolf, A., Swift, J. B., Swinney, H. L., Vastano, J. A., 1985. Determining Lyapunov exponents from a time series. Physica D: Nonlinear Phenomena 16 (3), 285–317.

Appendices

Appendix I: The Wigner function

In this appendix we provide three additional figures illustrating the Wigner function calculated around three vortices in a rotating BEC which contains three vortices and one anti-vortex after phase imprinting (see figures 1, 2 and 3). The anti-vortex is obtained by flipping the direction of circulation of a vortex at its original location in the condensate.

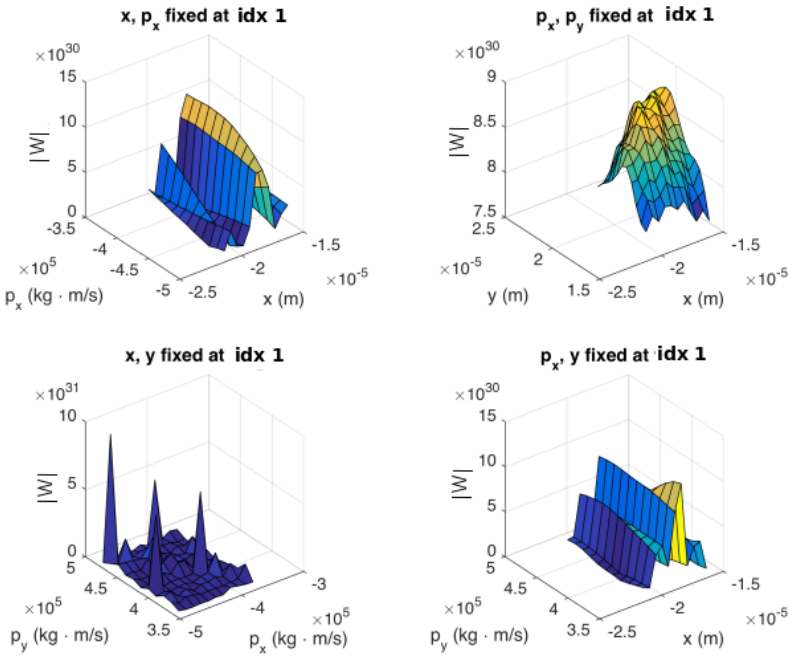

Figure 1: The calculated Wigner function, $W(x, y, p_x, p_y)$, around the vortex labelled index 1, 'idx 1', in a BEC with 3 vortices and 1 antivortex. The four plots of the absolute Wigner function $|W|$ are obtained by fixing y and p_y (upper left plot), x and y (upper right plot), p_x and p_y (lower left plot) and x and p_y (lower right plot) to their values at the vortex core.

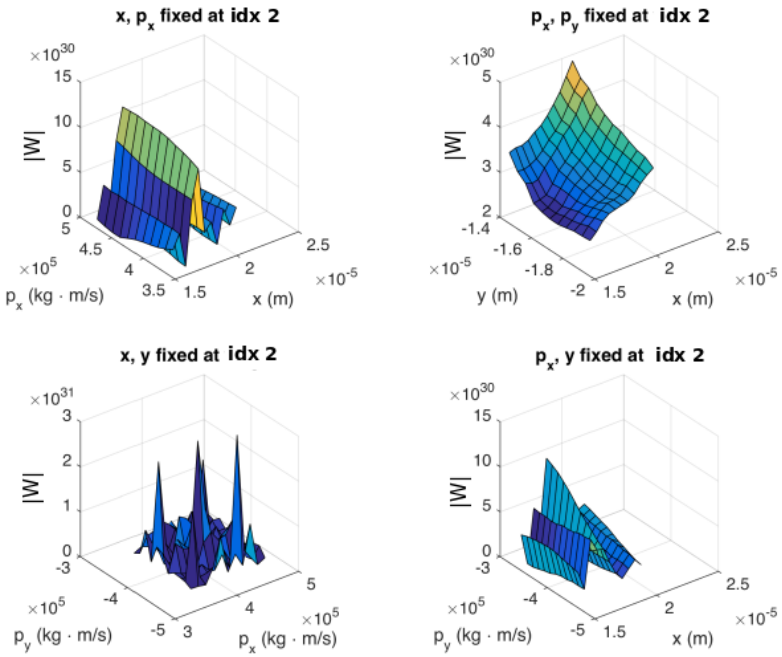

Figure 2: The calculated Wigner function, $W(x, y, p_x, p_y)$, around the vortex labelled by index 2, 'idx 2', in our simulated BEC with 3 vortices and 1 antivortex. The four plots of the absolute Wigner function $|W|$ are obtained by fixing y and p_y (upper left plot), x and y (upper right plot), p_x and p_y (lower left plot) and x and p_y (lower right plot) at the vortex core.

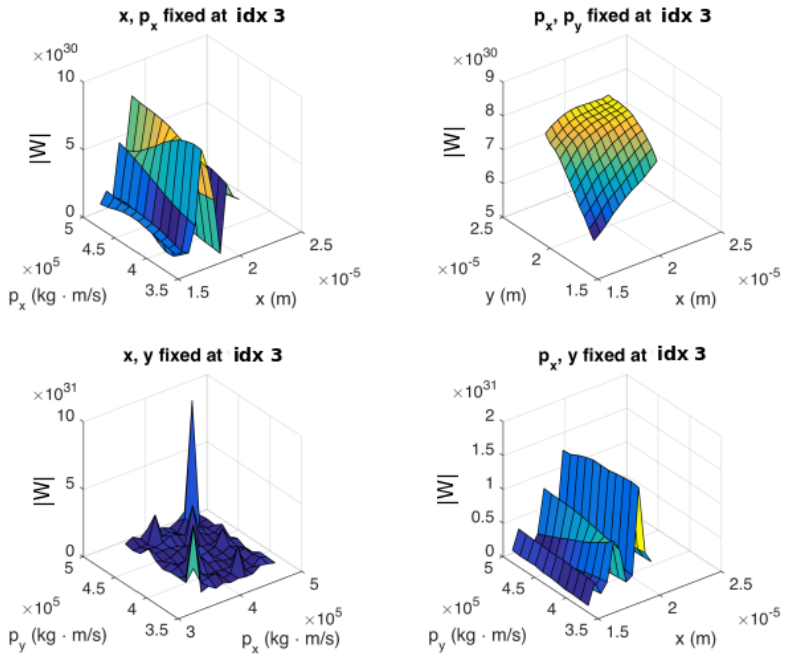

Figure 3: The calculated Wigner function, $W(x, y, p_x, p_y)$, around the vortex labelled as index 3, 'idx 3', in our simulated BEC consisting of 3 vortices and 1 antivortex. The four plots of the absolute Wigner function $|W|$ are obtained by fixing y and p_y (uppper left plot), x and y (upper right plot), p_x and p_y (lower left plot) and x and p_y (lower right plot) at the vortex core.